177
7/14/69

RECEIVED BY DTIE JUL 22 1969

885

MASTER

AEROSPACE
NUCLEAR
SAFETY

SC-CR-68-3677
July 1968

unclass
Kahn 7/17/69

STUDY OF SMALL PARTICLE ABLATION USING A FREE-FLIGHT RANGE

David K. Sangster
Gerald A. Shaw
AC Electronics-Defense Research Laboratories
General Motors Corporation

DISTRIBUTION OF THIS DOCUMENT IS UNLIMITED

P1996

SANDIA LABORATORIES

OPERATED FOR THE UNITED STATES ATOMIC ENERGY COMMISSION BY SANDIA CORPORATION | ALBUQUERQUE, NEW MEXICO; LIVERMORE, CALIFORNIA

Issued by Sandia Corporation,
a prime contractor to the
United States Atomic Energy Commission

Printed in the United States of America
Available from
Clearinghouse for Federal Scientific and Technical Information
National Bureau of Standards, U.S. Department of Commerce
Springfield, Virginia 22151
Price: Printed Copy $3.00; Microfiche $0.65

AEROSPACE SAFETY
TID-4500 (54th Edition)

SC-CR-68-3677

STUDY OF SMALL PARTICLE ABLATION USING A FREE-FLIGHT RANGE

Final Report

July 1968

Prepared by

David K. Sangster and Gerald A. Shaw
AC Electronics–Defense Research Laboratories
General Motors Corporation

for

Sandia Laboratories
under
Contract No. 48-6119

DISTRIBUTION OF THIS DOCUMENT IS UNLIMITED

ACKNOWLEDGEMENTS

The authors wish to acknowledge the contributions of Mr. R. A. Hayami for the design of the Fabry-Perot trigger system, Mr. Frank Ramsey for its fabrication, and Mr. John Serrano for its operation. The authors also wish to thank Mr. J. Oshiro for his aid in the operation of the laser shadowgraph systems.

CONTENTS

ILLUSTRATIONS

LIST OF SYMBOLS

A_{ng}, C_n, λ_{ng}	expansion coefficients and eigenvalues defined by Reference 7
B	ballistic coefficient (lb/ft^2)
C_D	drag coefficient
C_P	specific heat at constant volume, (BTU/lb-^{o}R)
g	acceleration of gravity (ft/sec^2)
$J_{u+1/2}$	half integral order Bessel function
K	thermal conductivity (BTU/sec-ft-deg R)
P_o	range pressure (atmos)
$P_n(X)$	legendre polynomial
Q_s	heating rate per unit area (BTU/ft^2-sec)
Q_{TOT}	integrated heat input to sphere (BTU)
r	nondimensional radius δ/R_n
Re	Reynolds number $= 2 R_n V\rho_\infty/\mu g$
R_n	radius of sphere (ft)
s	frontal surface area (ft^2)
t	time (sec)
$\overline{T}$	average sphere temperature with no melting (^{o}R)
T_{STAG}	stagnation point temperature of sphere (^{o}R)
T_{BACK}	temperature at back of sphere (^{o}R)
V	Velocity (ft/sec)
W	Weber number $\rho_\infty V^2 R_n/\sigma$
X	$\cos\theta$
α	thermal diffusivity $K/\rho_m C_p$ (sq ft/sec)
β	asymptotic temperature gradient in sphere (deg R): $R_n Q_s/K$
δ	distance from center of sphere (ft)
θ	angle between point on sphere and flight line
μ	viscosity lb-sec/ft^2
ρ_m	density of material (lb/ft^2)
ρ_o	density of gas at 1 atmos (gm/ℓ)
σ	surface tension (dyne/cm)
τ	non-dimensional time: $\alpha t/R_n^2$

STUDY OF SMALL PARTICLE ABLATION USING A FREE-FLIGHT RANGE

INTRODUCTION

Safety analysis for space nuclear power supplies requires a knowledge of the ablation behavior of microspheres of nuclear fuel when exposed to various reentry environments. The feasibility for full scale ablation testing of simulated fuel elements in a ballistic range under reentry conditions was demonstrated in a prior study at AC-DRL.(1)* The tests discussed in Reference 1 were made using microspheres of crystalline Al_2O_3 (synthetic sapphire) as a fuel simulant. Particles 400 microns to 700 microns in diameter were launched at velocities between 23,000 fps and 26,000 fps into air at pressures between 25 torr and 50 torr. The condition of the microspheres was determined from laser shadowgraphs and impact plates. Under these flight conditions the sapphire microspheres shattered due to thermal stress before any significant ablation could occur. However, the feasibility of launching such small particles at high velocities and obtaining in-flight photographic records of their shape-change was demonstrated.

For the follow-on study described in this report, flight conditions, microsphere sizes, and materials were selected (in conjunction with Sandia personnel) to demonstrate ablation mechanisms and to provide a check on the relationship of Weber number to the theory of liquid-layer stripping.(2) Sandia Corporation furnished all of the microspheres which ranged in size from 250 microns to 650 microns. The firings were done in four segments with ample time between each to evaluate the results before setting the flight conditions for subsequent segments.

---

* A list of references appears on page 49.

The material chosen as a fuel simulant for the first test series was sintered Al_2O_3. Eight microspheres were launched. The results of this series were inconclusive because of equipment malfunctions and the low degree of melt achieved on the particles during flight. The remaining three segments were accomplished by using gold microspheres in an effort to achieve the desired variation of Weber number together with a reasonable degree of melt in the test section. For the last two series of gold firings an attempt was made to obtain quantitative data on the ablation debris produced by installing cylindrical debris collectors in the range, coaxial with the flight line. The debris collectors were designed, fabricated, installed, and analyzed by Sandia personnel. The results of this phase of the experiments will be reported elsewhere.

RANGE AND INSTRUMENTATION

RANGE

The range configuration used for these tests is shown schematically in Figure 1.[*] A 30-caliber, 2-stage light gas gun capable of launching a single saboted microsphere at velocities from 18,000 fps to 25,000 fps is followed by a preflight chamber and an instrumented test section equipped with vacuum pumps. A port valve separates the test section from the preflight section so it is possible to have the two sections charged with different gases at different pressures prior to model launch. The effect of opening time on the actual flight conditions is discussed in Appendix A. The lengths of the flight sections for the four test segments and the location of the instrumentation are given in Table I.

INSTRUMENTATION

The basic range instrumentation consists of orthogonal spark shadowgraphs, laser shadowgraphs, an open shutter camera, and a single impact plate or impact plates in conjunction with Sandia debris collectors.

The orthogonal spark shadowgraph velocity stations are of conventional design. In the preflight section the sabot pieces trigger the interrupted light-screens. The microsphere in many cases is also in the field of view, and its velocity is determined too. In the test section the microsphere is by itself, and neither interrupted light-screens nor emission gas-cap radiation from the microsphere triggers gave reliable signals to activate the spark shadowgraph stations.

Three laser shadowgraphs (shown schematically in Figure 2) were installed in the test section to determine particle shape. These lasers in conjunction with Polaroid, Type 55 P/N film have an effective pulse duration in the order of 20 nanoseconds and the optical system has sufficient resolution to permit identification of particles as small as 20 microns. The trigger for starting to pump the laser is obtained from either a delayed signal from the gun, or from a delayed velocity station triggered by the sabot pieces. The trigger to Q-switch dump the laser, however, is difficult to obtain from microspheres flying through low ambient pressures.

---

[*] Illustrations begin on page 10.

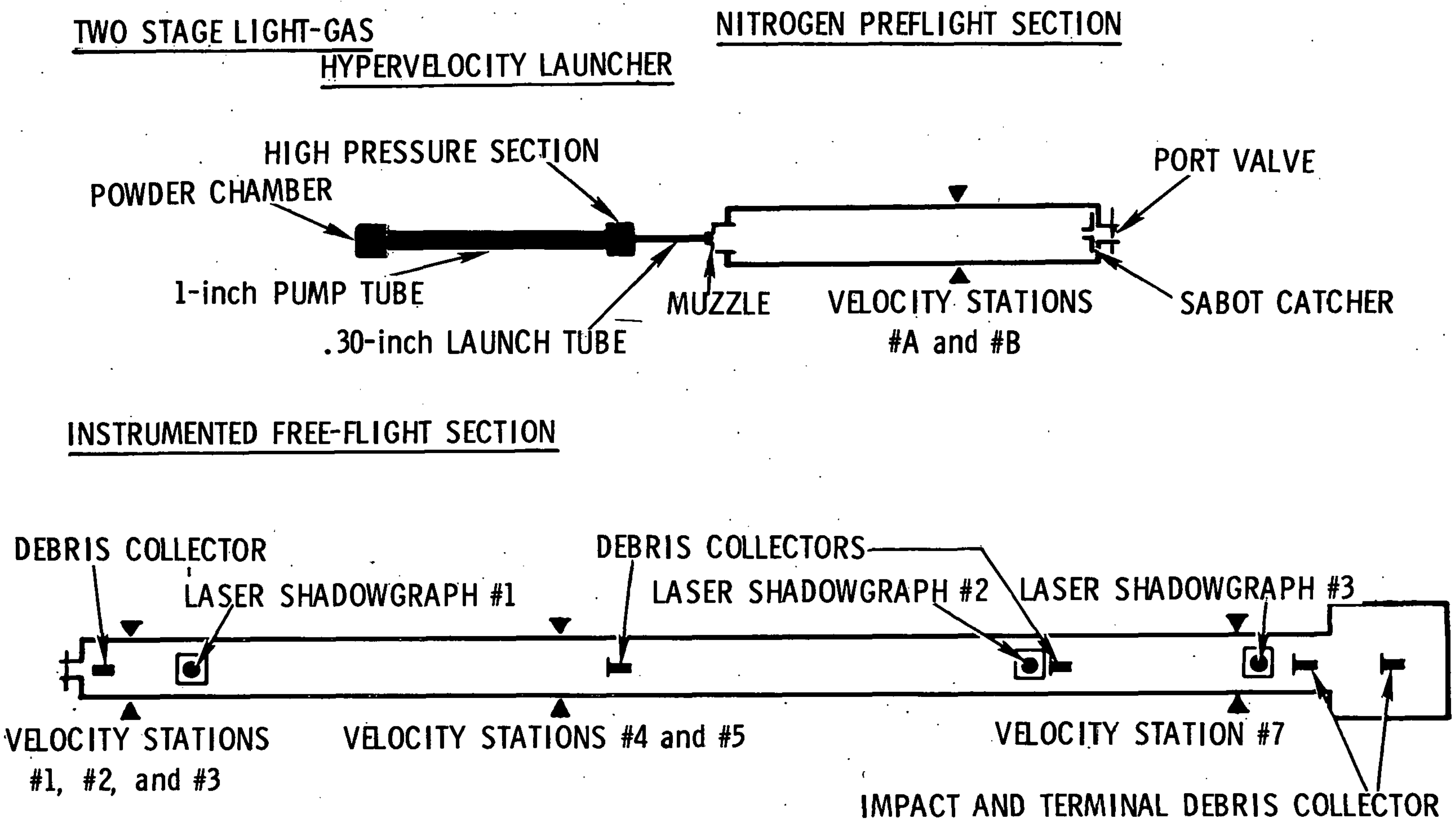

Figure 1. Range Configuration

Table I
DIMENSIONS OF INSTRUMENTED FREE-FLIGHT RANGE

Segment of Tests	Port Valve (preflight length)	Laser Shadowgraphs (from muzzle)			Debris Collectors	Impact	Flight Length
		#1	#2	#3			
1	not used	31'	90'	106'	- - -	119'	119'
2	not used	31'	90'	106'	- - -	119'	119'
3	23'	31'	90'	106'	27' 93' 108'	118'	95'
4	27'	35'	94'	112'	87' 96' 114'	120'	93'

Highly tuned interrupted light-screen triggers were installed for the first segment of the program and they proved to be unreliable, yielding only one laser shadowgraph from the eight rounds. For the second segment of the tests, a Fabry-Perot microwave cavity-resonator (normally used to measure electron densities in plasmas) was installed as a trigger for Q-switching laser #3. The results were very encouraging and shadowgraphs of ablating gold microspheres were obtained. Based on these results, three higher frequency microwave resonators were fabricated and installed to Q-switch all three lasers. The results in test segments three and four were somewhat disappointing, due in part to the large shot dispersion encountered with the very small microspheres. The microwave beam is relatively small (approximately 2 in. dia.) and the dispersion on some shots exceeded this. On other shots, the particles were highly ablated at the laser stations and the particles passing the trigger were only a small fraction of their original size. Nonetheless, triggers were obtained from several 250-micron particles, and this new application of the Fabry-Perot resonator could doubtless be developed to a far higher degree than was possible within the limited scope of this program.

The Sandia debris collectors were cylindrical tubes with end plates having holes for the model to pass through. The final debris collector had a solid polished aluminum impact plate at the back end. The collectors were accurately installed on the range so their centerline corresponded to the anticipated flight path of the model. In the absence of the debris collectors, a single polished aluminum impact plate was installed at the end of the range.

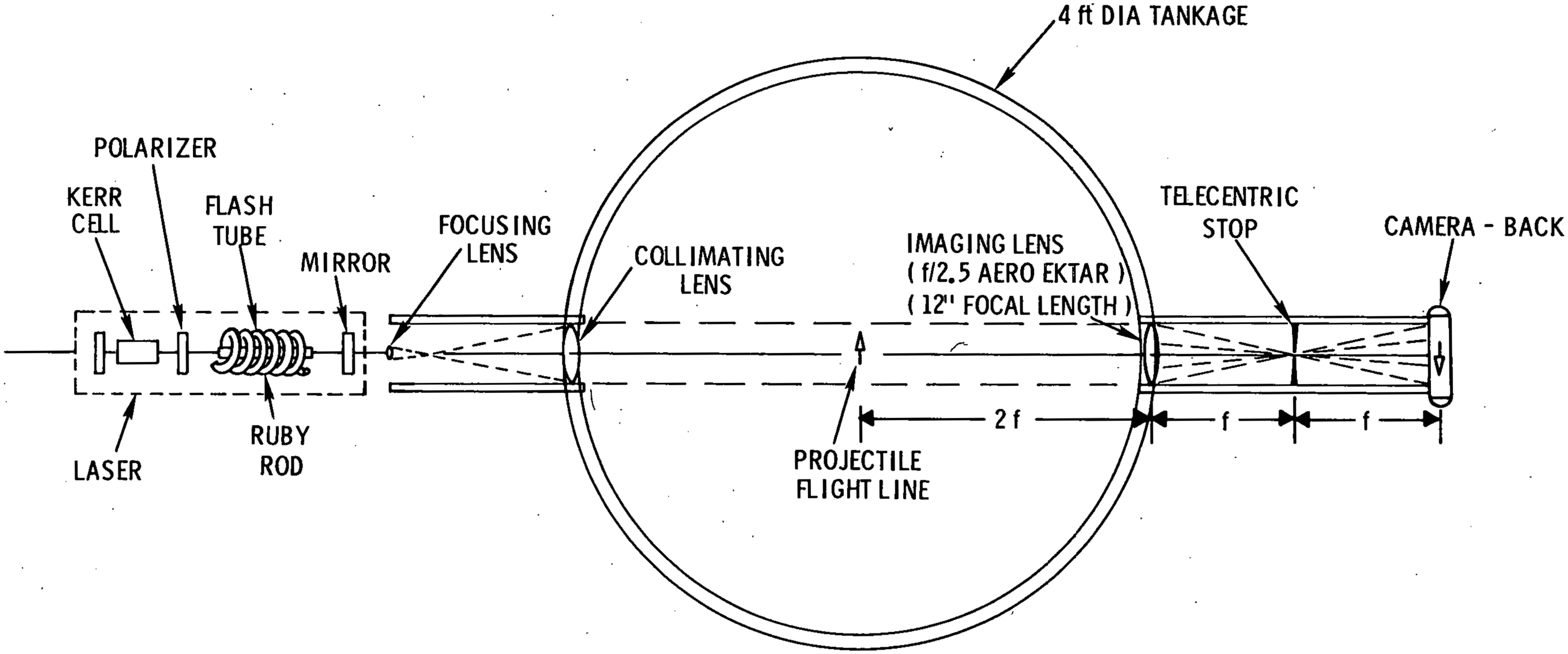

Figure 2. Schematic of Laser Shadowgraph Station

EXPERIMENTAL PROGRAM

Al_2O_3 MICROSPHERES — FIRST SEGMENT

Flight conditions and impact observations are given for all rounds of the first test segment in Table II. The tests using the 400-micron Al_2O_3 microspheres showed no melt breakup and no thermo-mechanical breakup for initial velocities of 20,000 fps and range pressures of 3- to 10-mm Hg of air (Weber Nos. 57 to 183).

GM predictions of deceleration, heating rate, and temperature for the 400-micron Al_2O_3 microspheres (Rounds 8B73, 8B82, and 8BX21) are shown in Figures 3, 4, and 5. The prediction method is described in Appendix B. In all tests the body temperature at the stagnation point does not reach melt temperature ($4160^{\circ}F$). Due to the low density of material, velocity and heating rates are attenuated rapidly, and sufficient heating does not occur. For these velocities and microsphere sizes, neither increasing the length of the range nor changing flight pressures will increase temperatures up to melt. Either the microsphere must be ballasted to maintain high velocities and heating rates, or initial velocity and microsphere size must be increased to obtain melt temperatures at the surface. Both these changes tend to increase Weber Number, which is contrary to the test objectives that favor the low Weber No. regimes. Both Sandia Corporation and Martin-Marietta performed more elaborate computer predictions for these flight conditions that indicated very slight melting at impact — too little to be resolved on the shadowgraphs. The inability to provide significant particle melting at Weber numbers of interest was a primary reason for switching to gold for the remainder of the program.

No attempts to launch 200-micron Al_2O_3 microspheres were made because emission detector and interrupted light-screen trigger signals from the 400-micron Al_2O_3 microspheres were difficult to obtain, and difficulties in launching the very small, low density Al_2O_3 microspheres were expected. No shadowgraphic data were obtained except for one picture (Figure 6) of an intact 400-micron microsphere (test 8B80) shortly after launch. Single clean impacts were obtained on the polished aluminum impact plates on tests 8B73, 8B81, 8B52, and 8BX21 (Figures 7, 8, 9 and 10). An attempt was made to catch the microsphere in flight by Martin-Marietta personnel. A soft catcher stuffed with cotton was used on test 8B74. The thin plastic cover of the catcher should, however, shatter the microsphere at such high velocities, and further attempts at catching the microsphere intact were not deemed feasible.

Table II
FIRST SEGMENT — ALUMINA MICROSPHERES

AC Test No.	Diameter (microns)	Range Pressure (mm Hg)	Initial Velocity (ft/sec)	Impact Comments
8B70	400	NIL	—	Launch malfunction.
8B71	400	5	—	Launch malfunction.
8B72	400	3	20,300	Microsphere lost at sabot catcher.
8B73	400	3	20,200	1100-0 Al plate — 1 clean impact.
8B74	400	3	20,400	Martin — soft catcher — no report.
8B80	400	3	20,650	1100-0 Al plate — 1 clean impact.
8B81	400	5	20,600	1100-0 Al plate — 1 clean impact. (1 small impact due to low velocity piston piece.)
8B82	400	5	19,650	1100-0 Al plate and streak camera — 1 clean impact, no in-flight luminosity recorded.
8BX19	400	10	20,000	Launch malfunction.
8BX20	400	10	20,300	1100-0 Al plate and streak camera — 1 clean impact, no in-flight luminosity.
8BX21	800 (sapphire)	15	25,250	1100-0 Al plate and streak camera — severe thermo-mechanical breakup and bright in-flight luminosity.
8BX22	800 (sapphire)	7	24,650	1100-0 Al plate and streak camera — severe thermo-mechanical breakup and bright in-flight luminosity.

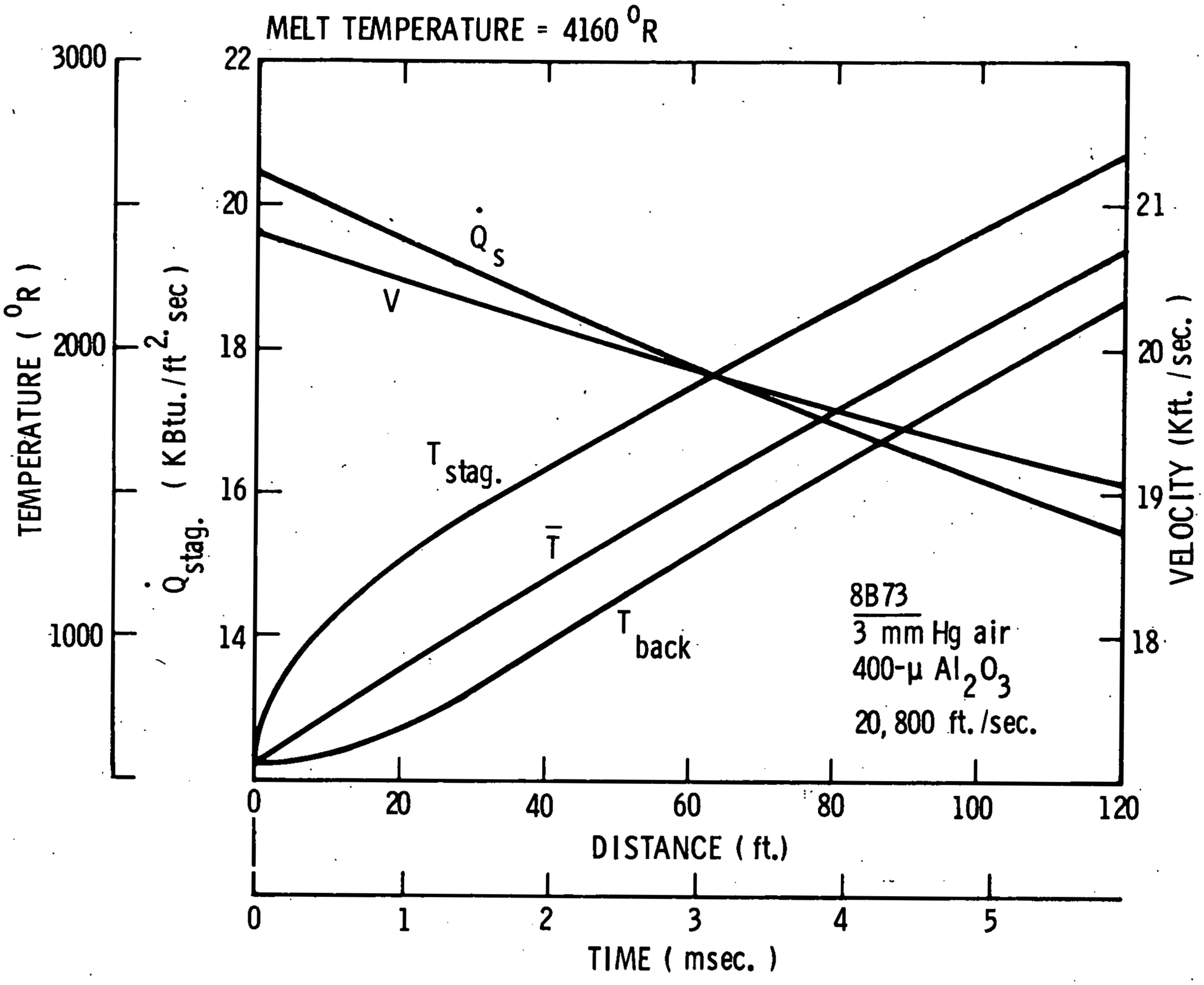

Figure 3. Flight Dynamics and Heating (8B73)

A focused, open-shutter camera recorded the impact flash on the three experimental tests: 8BX20, 8BX21, and 8BX22, (Figure 11). Note that no in-flight luminosity was recorded on the fast (10, 000 speed Polaroid) film on test 8BX20. The test 8BX21 of an 800-micron sapphire microsphere, which undergoes severe mechanical breakup due to thermal stresses,(1) is seen to be very luminous. The trajectories and impacts of many ablation products are seen in the open-shutter photograph. The test 8BX22 of an 800-micron sapphire microsphere was launched into lower pressures such that the velocity attenuation of debris is less than in test 8BX21, resulting in greater in-flight luminosity at the end of the range.

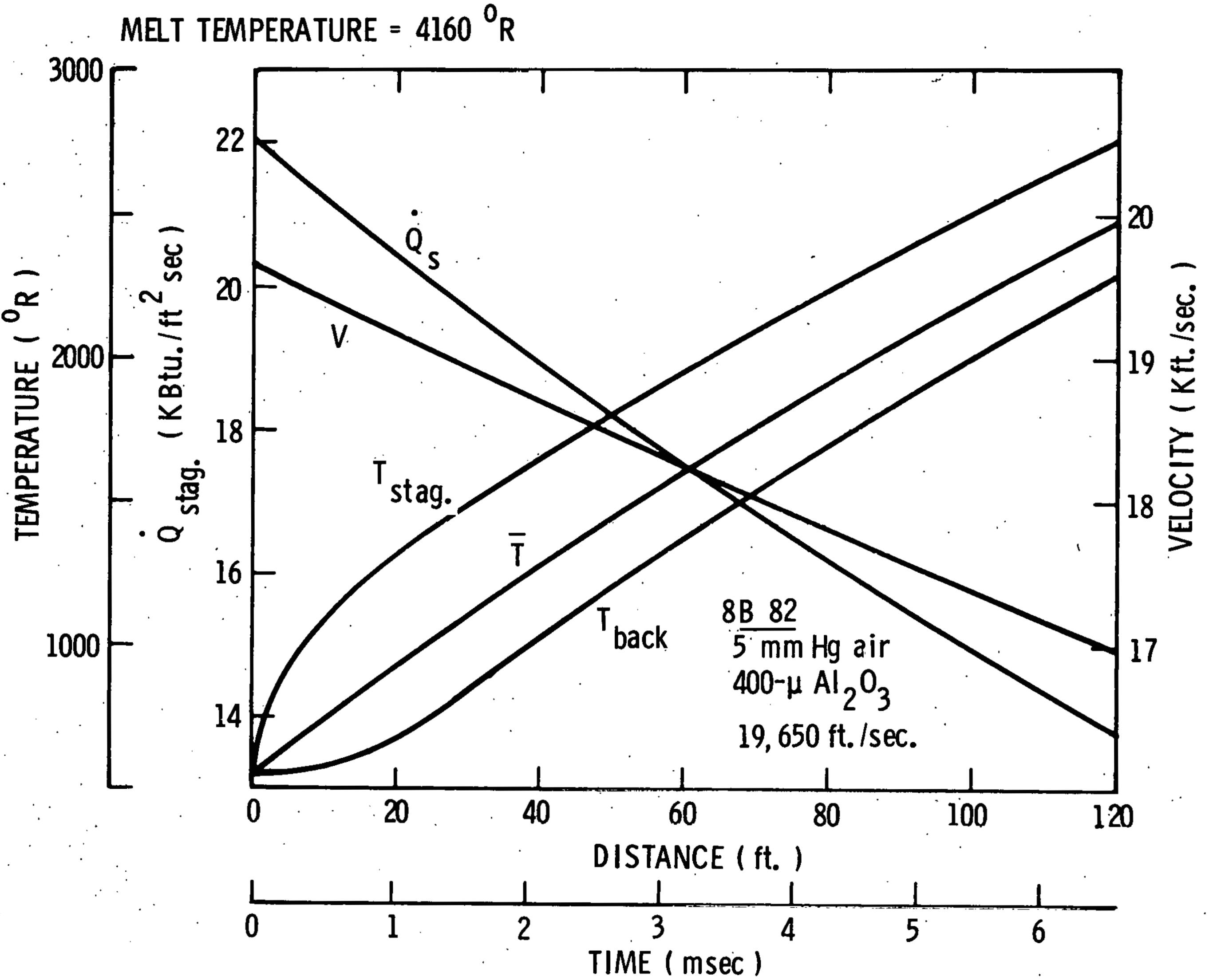

Figure 4. Flight Dynamics and Heating (8B82)

GOLD MICROSPHERES — SECOND SEGMENT

Flight conditions and impact observations for the first gold series are given in Table III. Flight conditions for this segment were selected to provide significant melting of the microspheres at Weber numbers between 20 and 150. The gold microspheres proved to be much easier to launch than the lighter Al_2O_3 particles of the same diameter and very good impact data of the main particle and of ablation products were obtained. Triggering difficulties continued to limit shadowgraphic data, but some laser shadowgraphs of intact and rapidly ablating gold microspheres were obtained by using the microwave resonant-cavity trigger. Seven rounds were fired in this series, which was considered sufficient for the high Weber number tests.

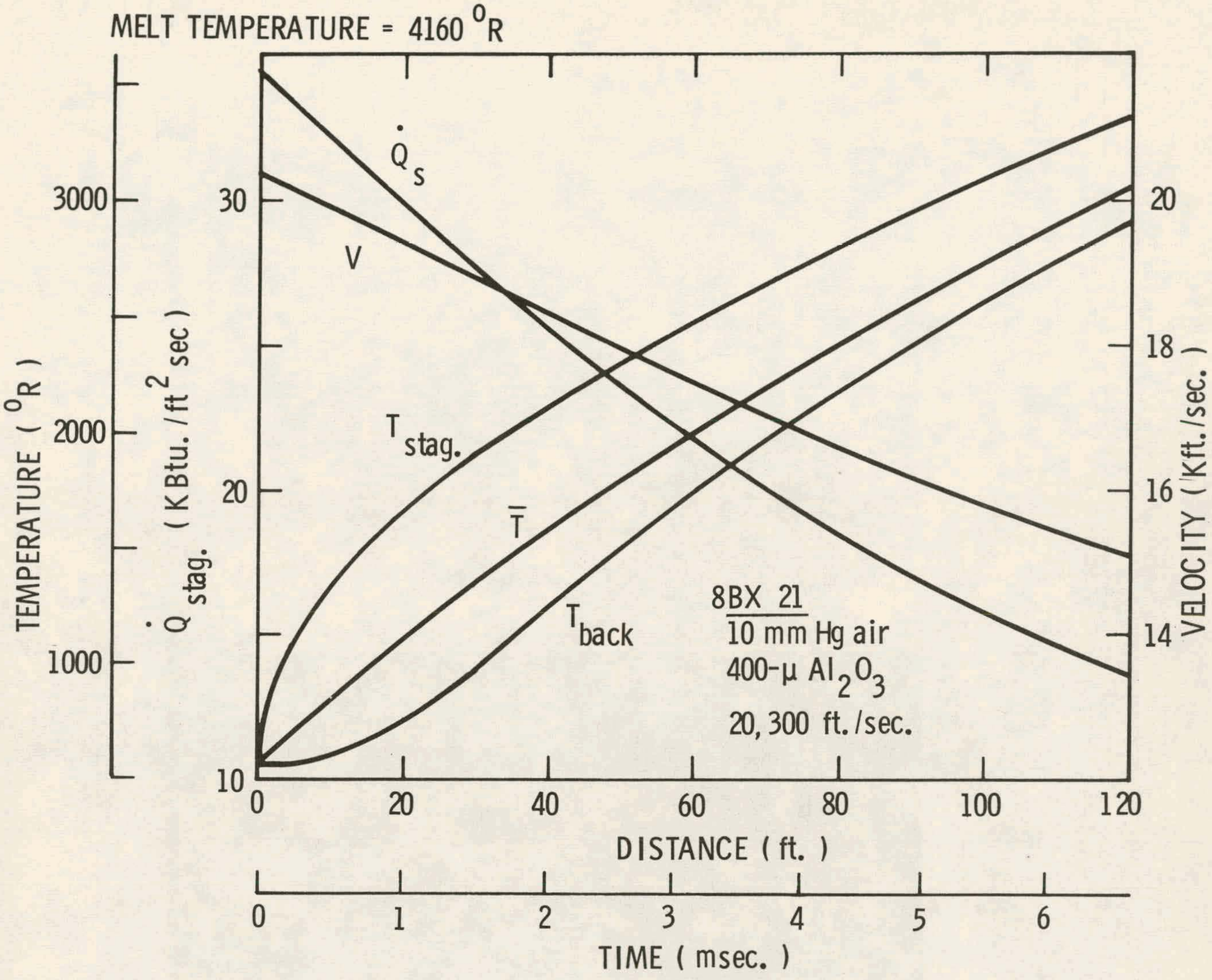

Figure 5. Flight Dynamics and Heating (8BX21)

GOLD MICROSPHERES — THIRD SEGMENT

The two pressure / two gas range configuration was used for this and the following test series. Nitrogen was used in the preflight section and air, at a lower pressure was used in the test section. The controls were arranged so that the port valve, when fully opened, fired the gun. The time from actuation of the port valve to model launch is about one second and, as shown in Appendix A, no shock is propagated into the low pressure test section. Also, an upper limit for the increase in test section pressure during this time is shown in Appendix A to be about 18% with a corresponding drop in preflight pressure of about 8%. Neither of these pressure changes is negligible but they are upper limits and should not have a major influence on the two governing parameters of heating rate and Weber number.

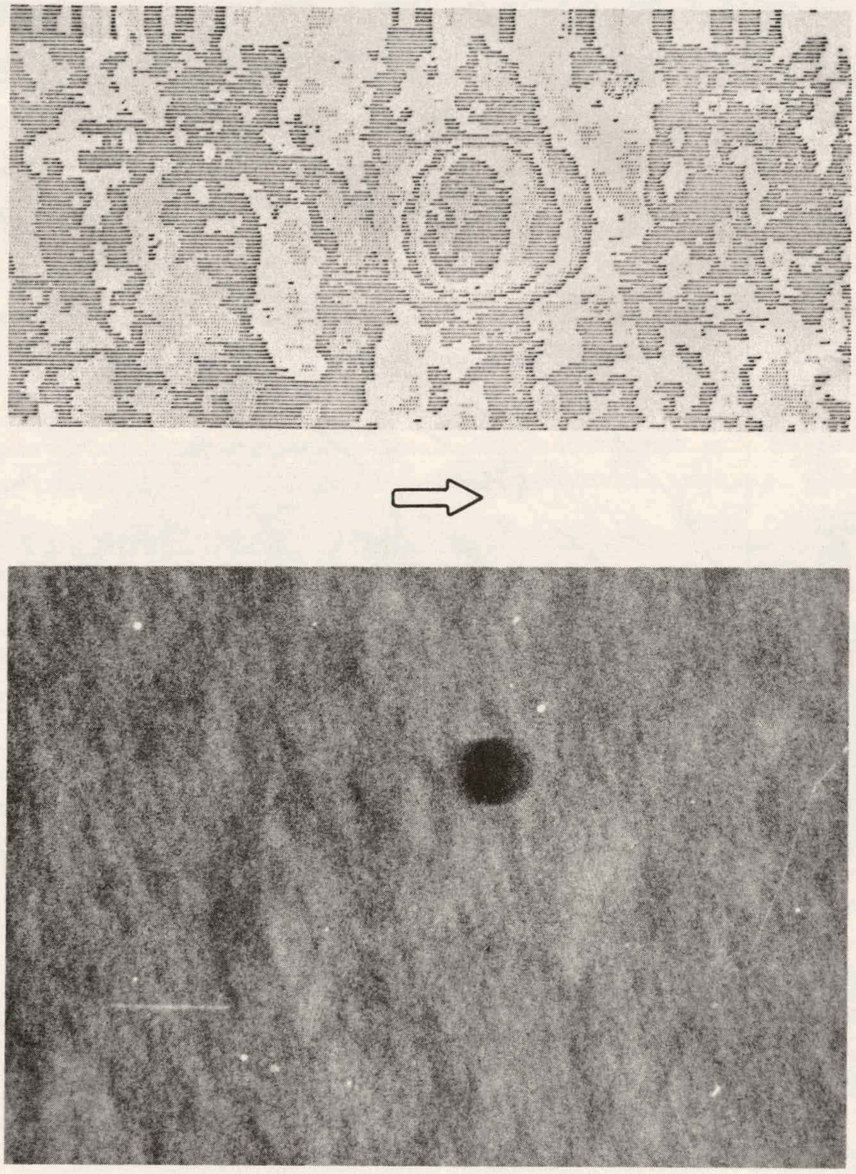

Figure 6 Laser Shadowgraph #4, 400-Micron Al_2O_3 (sintered) Microsphere and Isodensitometer Trace (8B80)

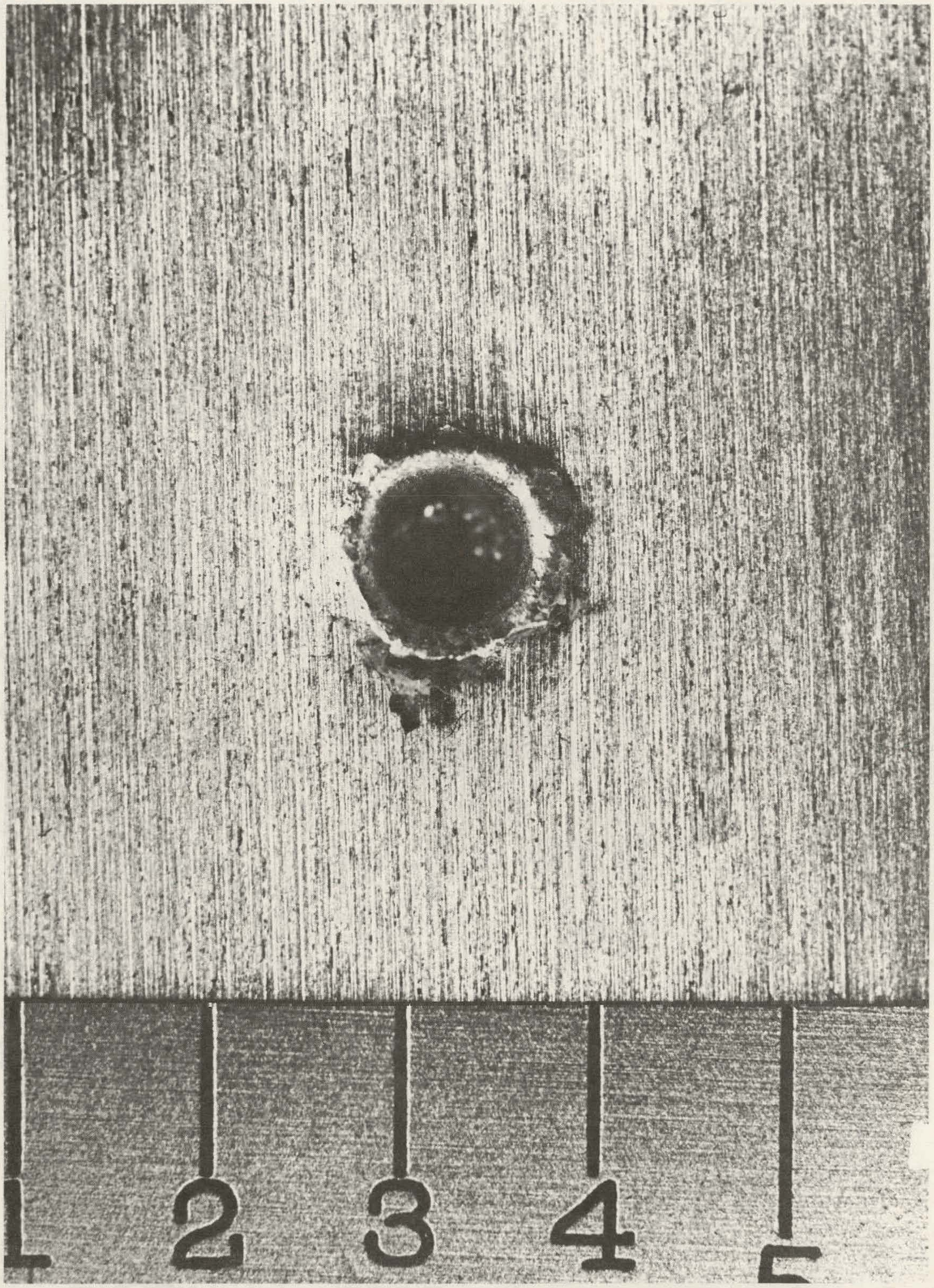

Figure 7 Impact Plate — 400-Micron Al_2O_3 (sintered) Microsphere (8B73)

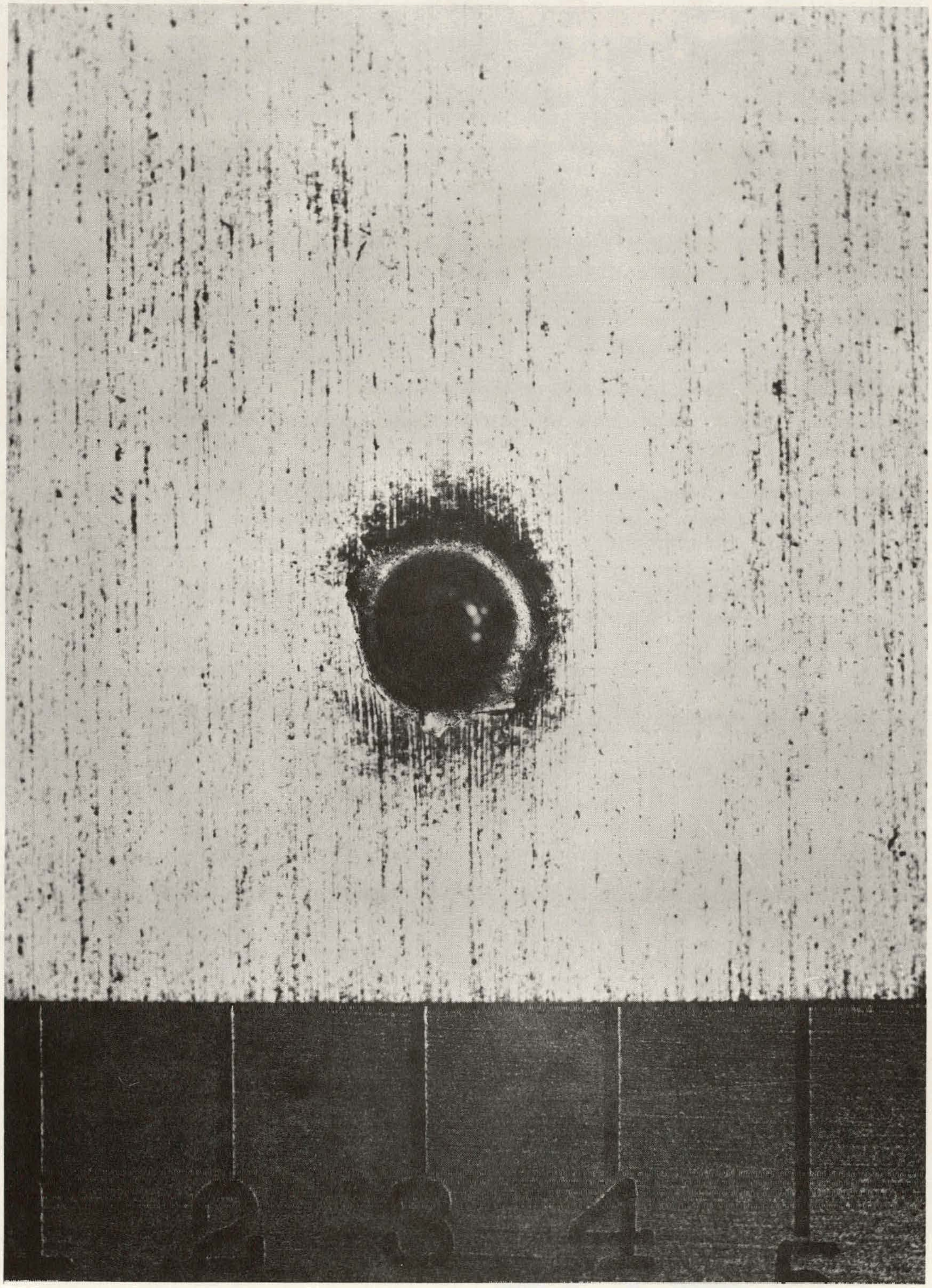

Figure 8 Impact Plate — 400-Micron Al_2O_3 (sintered) Microsphere (8B80)

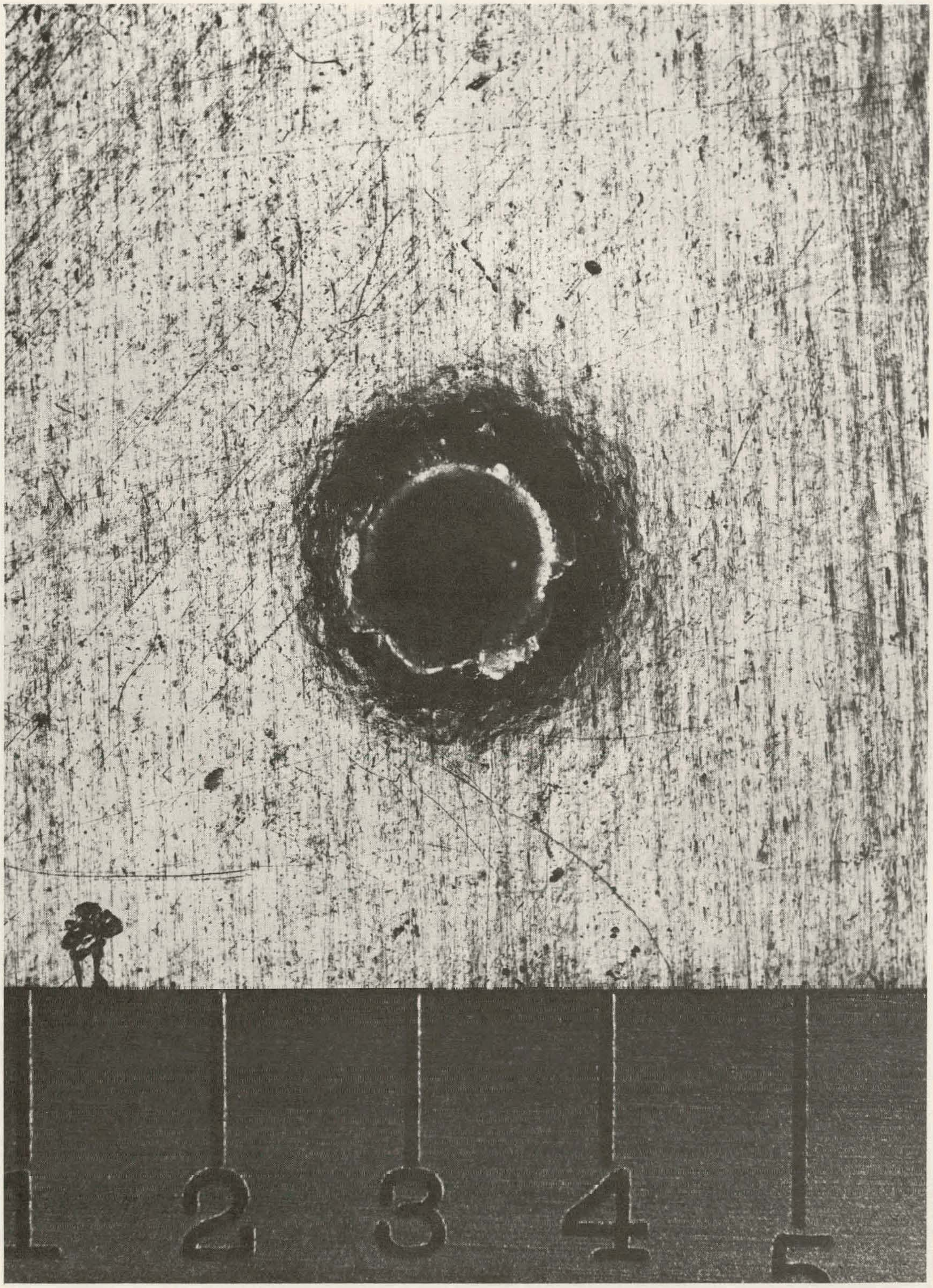

Figure 9 Impact Plate — 400-Micron Al_2O_3 (sintered) Microsphere (8B81)

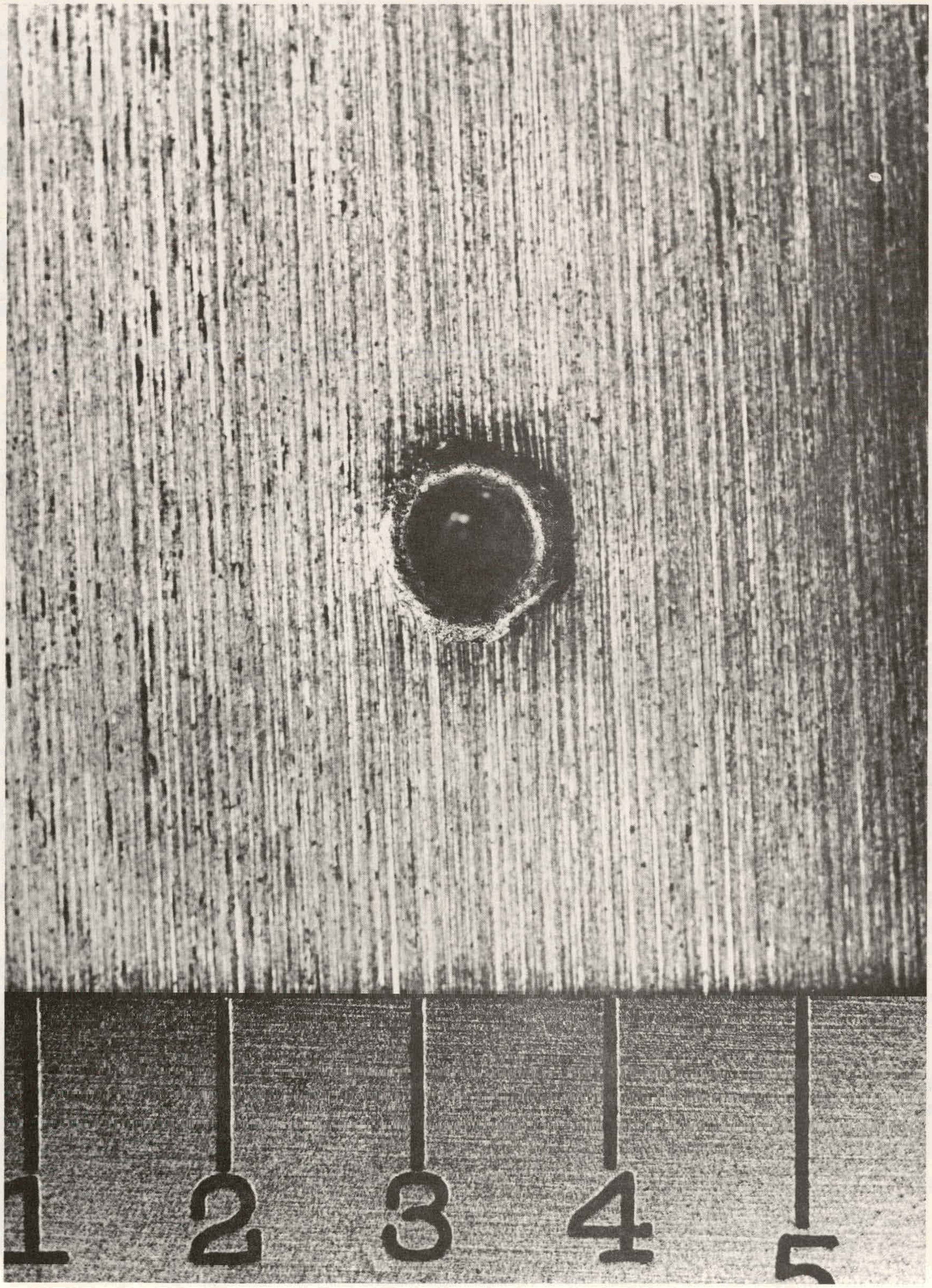

Figure 10 Impact Plate — 400-Micron Al_2O_3 (sintered) Microsphere (8B82)

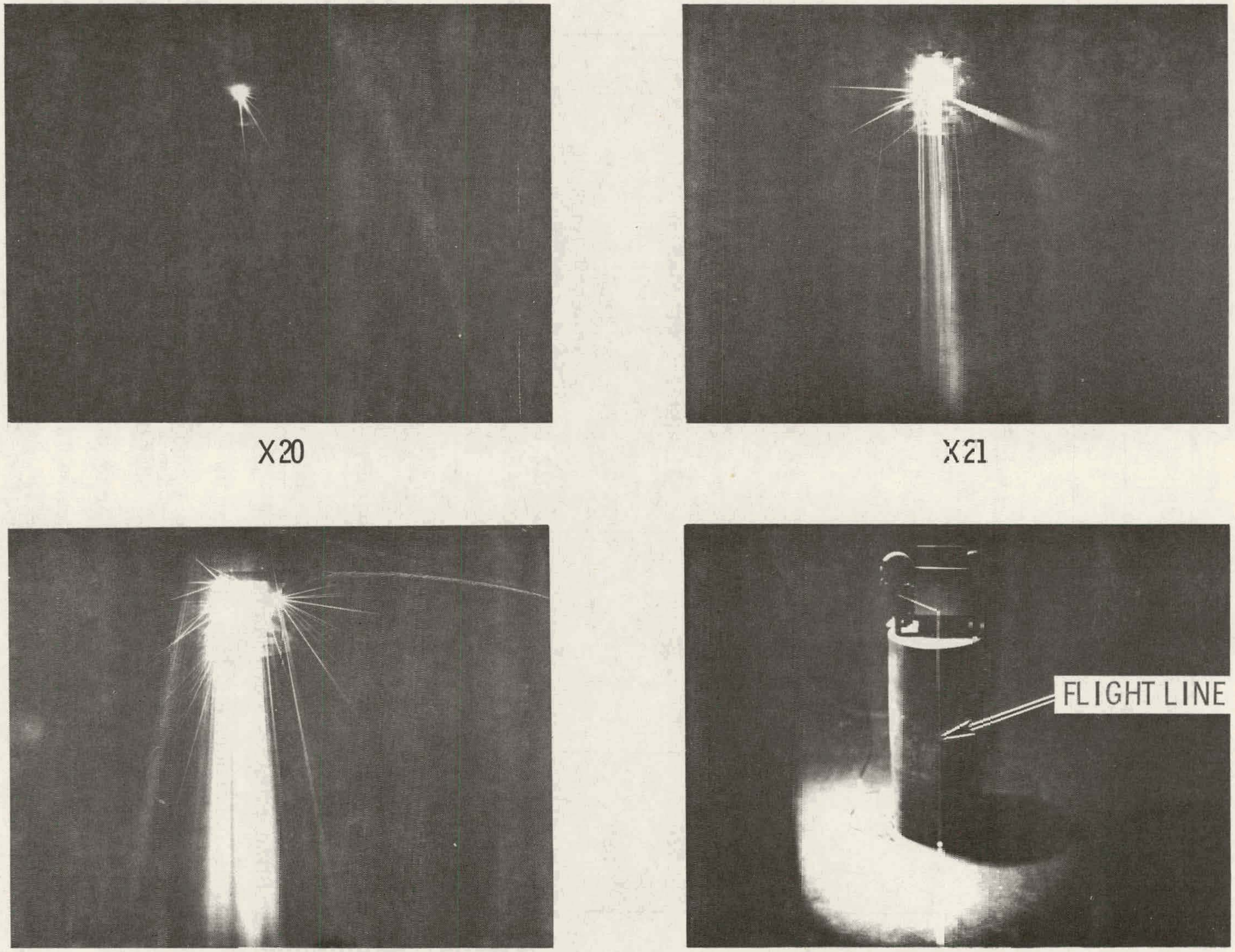

X20

X21

X22

STATIC

Figure 11 Open Shutter Camera Records — BX20, BX21, BX22, and Static

Table III
SECOND SEGMENT – GOLD MICROSPHERES

AC Test No.	Diameter (microns)	Range Pressure (mm Hg)	Initial Velocity (ft/sec)	Impact Comments
8B157	650	8	21,600	1100-0 Al plate – 1 main and fine debris impacts.
8B158	650	8	21,800	1100-0 Al plate – 1 main and fine debris impacts.
8B159	520	7	21,800	1100-0 Al plate – 1 irregular main, fine debris and vapor flash impacts.
8B160	520	7	21,800	1100-0 Al plate – 1 irregular main, fine debris and vapor flash impacts.
8B161	520	2	21,900	1100-0 Al plate – 1 clean impact.
8B162	380	6-7	21,500	1100-0 Al plate – fine debris impacts.
8B163	380	2	22,000	1100-0 Al plate – 1 main and fine debris impacts.

Flight conditions were selected to provide adequate melting in the test section in combination with nominal Weber numbers of 5, 7-1/2, and 10. Eight rounds were fired and the test conditions and impact comments are listed in Table IV. Sandia debris collectors were installed on all but one round of this series, as shown in Figure 12. With these smaller microspheres, shot dispersion increased, and in several tests they impacted on the front face or on the inside edge of the first collector. The results of this segment indicated some desirable changes in the design of the debris collectors. The paucity of laser triggers also indicated less sensitivity from the Fabry-Perot trigger system than was anticipated.

Table IV
THIRD SEGMENT — GOLD MICROSPHERES
(23' Preflight/Flight)

AC Test No.	Diameter (microns)	Range Pressure (mm Hg)	Initial Velocity (ft/sec)	Impact Comments
8B216	380	12 N/1 Air	22,500	1100-0 Al plate — 1 clean impact.
8B217	380	12 N/4 Air	22,150	Sandia Collectors — 1 irregular main and fine debris impacts in impact debris collector.
8B218	380	15 N/1 Air	22,700	Sandia Collectors — 1 main and fine debris impacts on collector face (steel) — 93 ft.
8B219	380	8 N/1 Air	18,500	Microsphere lost in displaced filter paper of collector close to port valve.
8B220	380	8 N/1 Air	16,300	Sandia Collectors — 1 main and fine debris impacts in impact debris collector.
8B221	380	12 N/1 Air	22,200	Sandia Collectors — 1 main and fine debris impacts at collector inside face (filter paper)— 93 ft.
8B222	250	8 N/1 Air	22,400	No trace of microsphere
8B223	380	12 N/1 Air	22,150	Sandia Collectors — 1 main and fine debris impacts on edge of collector (steel) — 93 ft.

GOLD MICROSPHERES — FOURTH SEGMENT

This final test series was designed to repeat the low Weber number firings of the third segment with improved debris collectors and laser triggers. Larger (2-inch) holes were used in the debris collectors and polished aluminum impact plates were installed on the face of each collector. Flight conditions and impact observations for this series are listed in Table V. Good impact data was obtained for the Weber numbers 10 and 7-1/2 conditions and partial data obtained for the Weber number 5 condition. For the 250-micron spheres shot dispersion appeared to increase to

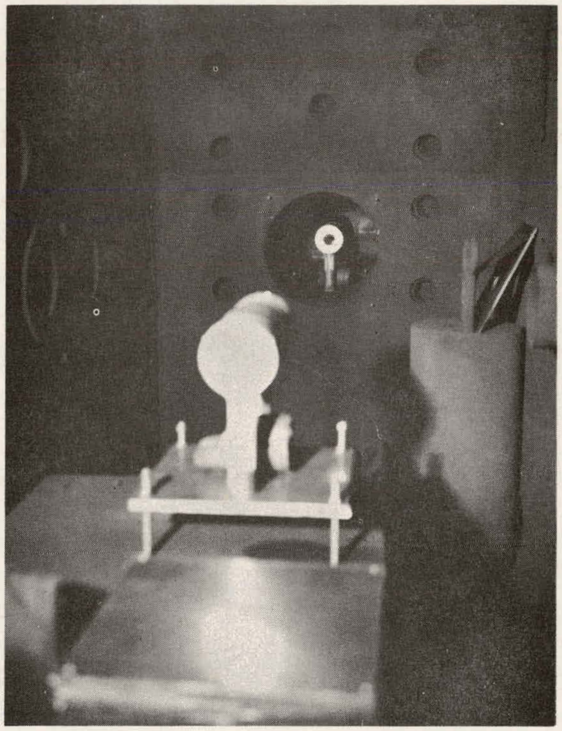

Figure 12 Final Ablation Debris Collector and Impact Debris Collector at End of Range

Table V
FOURTH SEGMENT — GOLD MICROSPHERES WITH SANDIA DEBRIS COLLECTORS

AC Test No.	Diameter (microns)	Range Pressure (mm Hg)	Initial Velocity (ft/sec)	Impact Comments
8B226	380	12 N/4 Air	22, 200	Fine and small debris impacts on all collectors, no main impact.
8B227	380	15 N/1 Air	21, 600	1 main, fine and small debris and vapor flash impacts at first collector — 77 ft.
8B228	380	15 N/1 Air	21, 800	No trace of microsphere.
8B229(X)	520	15 N/1 Air	22, 100	Microsphere impacted at sabot trap.
8BX45	520	15 N/1 Air	22, 700	Microsphere impacted at sabot trap.
8BX46	520	15 N/1 Air	22, 300	1100-0 Al ring — 1 main, fine and small debris impacts — 120 ft.
8B230(X)	250	7 N/1 Air	23, 000	2 large and many small debris impacts at first collector used — 96 ft.
8B231	250	7 N/1 Air	22, 900	1 main and many small debris impacts at first collector used — 96 ft.
8B232	250	7 N/1 Air	23, 000	1 main and many small debris impacts at first collector used — 96 ft.
8B233	250	7 N/1 Air	22, 850	1 main (on impact plate) and many small debris impacts on all collectors.
8B234	380	15 N/1 Air	22, 900	1 main (on impact plate) and many fine and small impacts on all collectors except on first — 96 ft.
8B235	250	12 N/1 Air	18, 200	1 clean main impact at first collector used — 96 ft.

accommodate the larger opening provided in the debris collectors and several tests impacted on the first collector. Again, little information was obtained on the laser shadowgraphs due to shot dispersion and the heavy ablation experienced by the particles. In most cases, after the first laser station, the main particle had ablated into many, much smaller particles, which would not trigger subsequent lasers.

DISCUSSION OF RESULTS

LASER SHADOWGRAPHIC DATA OF ABLATING GOLD MICROSPHERES

Although the laser shadowgraphic data is quite limited, good records were obtained that show the ablation mechanisms of the large (520- and 650-micron) gold microspheres. Figure 13 (test 8B158) is a 650-micron gold microsphere after 108 ft of free-flight in 8-mm Hg air. Some evidence of liquid layer stripping is seen. Figure 14 (test 8B159 at 108 ft) is a 520-micron gold microsphere. The model appears hemispherical and has undergone moderate ablation. Figure 15 shows a severely ablated 520-micron gold microsphere in sharp focus (test 8B160 at 108 ft). Very thin threads of gold extend back from the main particle, and ablation debris is seen in the wake. Triggers were obtained on the smaller (380- and 250-micron) gold spheres only before they started to ablate. Two records of intact small microspheres were obtained (Figures 16 and 17 tests 8B163, 8B233).

GENERAL DISCUSSION OF GOLD ABLATION DATA OBTAINED FROM IMPACT PLATES

An extensive quantitative analysis of the impact plates is being done by Sandia, so this report will include only general remarks on the experimental data derived from them. During the first segment of gold microsphere tests, impact records of microspheres in various degrees of ablation were obtained. Tests 8B161 and 8B216, (Figures 18 and 19) impacted in one piece and there were no ablation debris impacts. Tests 8B157, 8B158, and 8B220 (Figures 20, 21 and 22) were partially ablated; several very small impacts are seen around and inside the main impact. Test 8B163 (Figure 23) had, in addition to the smaller impacts, slight evidence of a hot vapor cloud following the microsphere. There was severe ablation on tests 8B159 and 8B160 (Figures 24 and 25), and a distinct discoloration around the impact indicates a hot vapor cloud of ablation debris followed the model. Many small impacts are seen and there is a complete distribution of very fine impacts. Test 8B217 (Figure 26) has undergone severe ablation and breakup, although some large particles do impact. The shadow effect of the 1-3/4-inch hole of the impact debris collector through which the particle passed is seen as an arc. Test 8B162 (Figure 27) was totally broken up — the impact plate was peppered with small impacts. No evidence of a concentrated vapor cloud reached the impact plate, indicating that the microsphere had disintegrated well in advance of the impact plate, and that the vapor cloud as well as very small debris were attenuated.

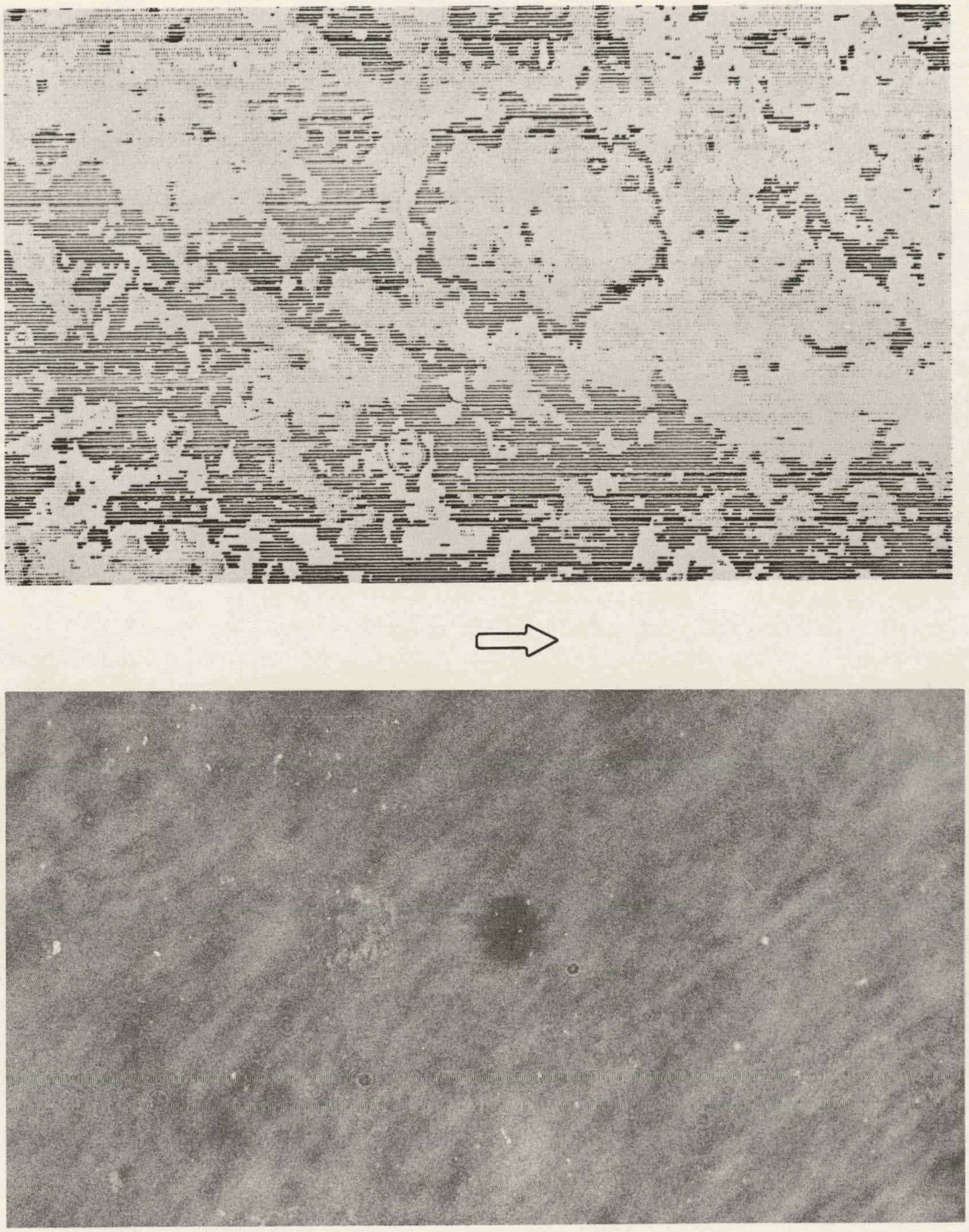

Figure 13 Laser Shadowgraph #3, 650-Micron Gold Microsphere and Isodensitometer Trace (8B158)

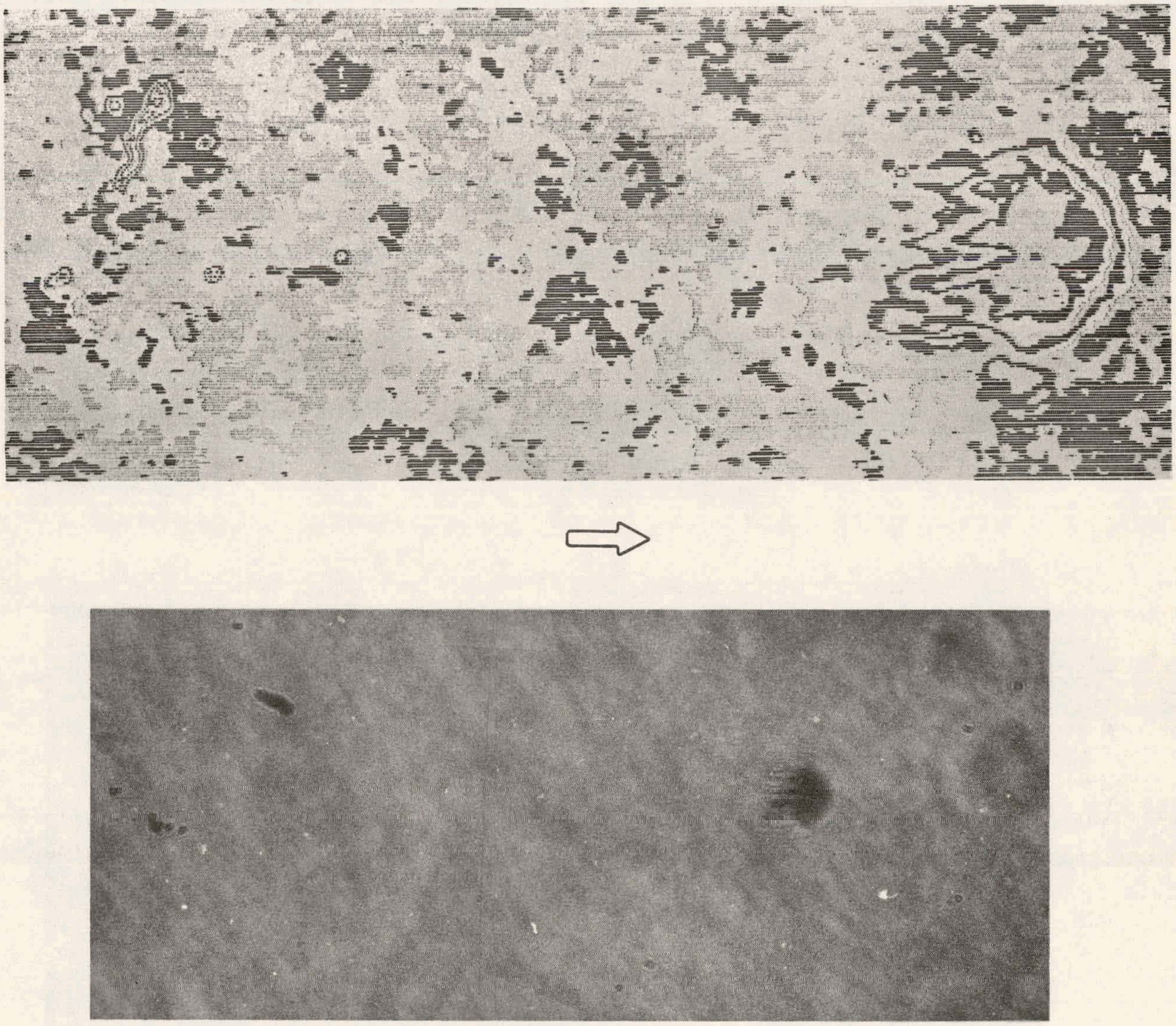

Figure 14 Laser Shadowgraph #3, 520-Micron Gold Microsphere and Isodensitometer Trace (8B159)

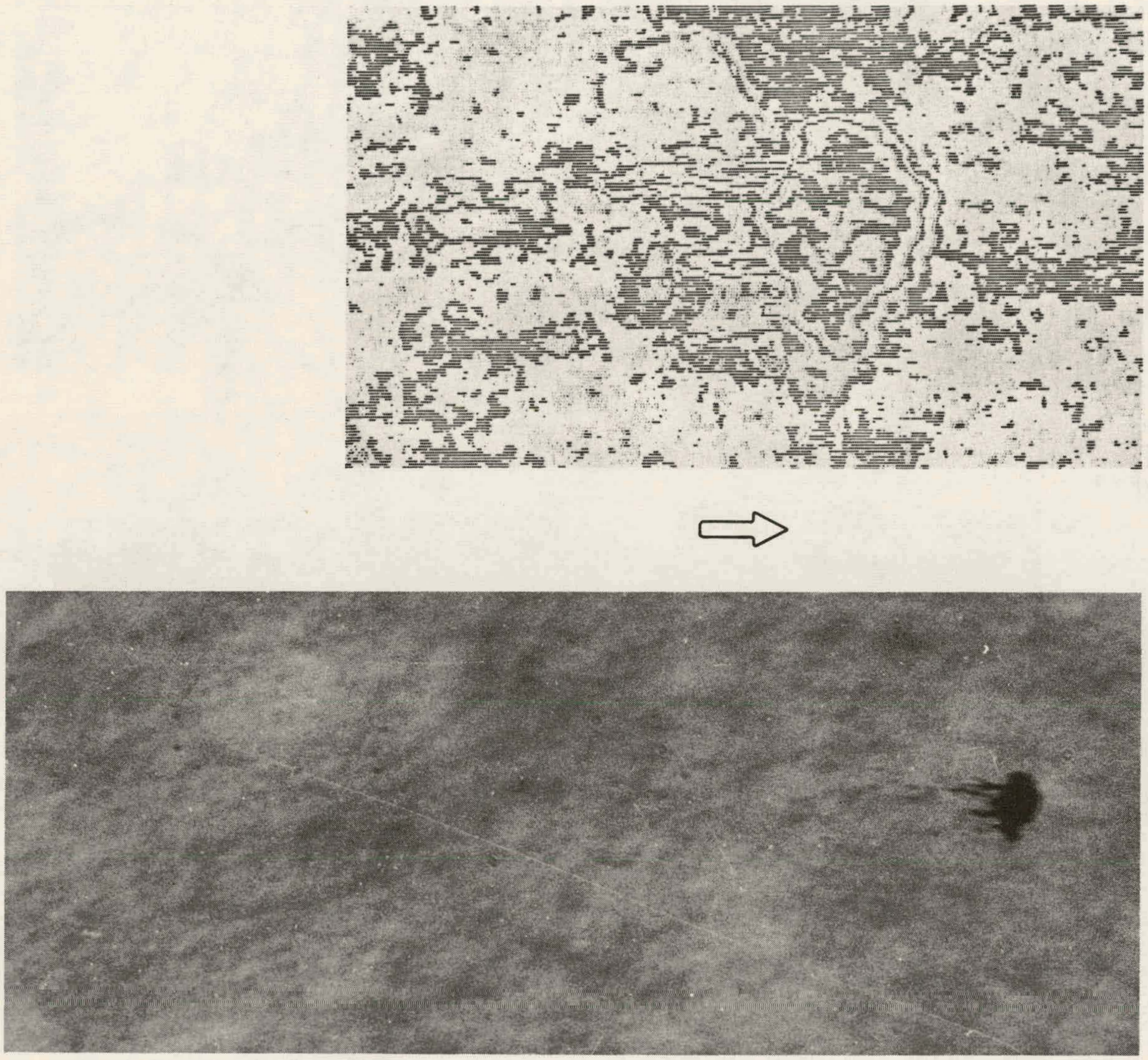

Figure 15 Laser Shadowgraph #3, 520-Micron Gold Microsphere and Isodensitometer Trace (8B160)

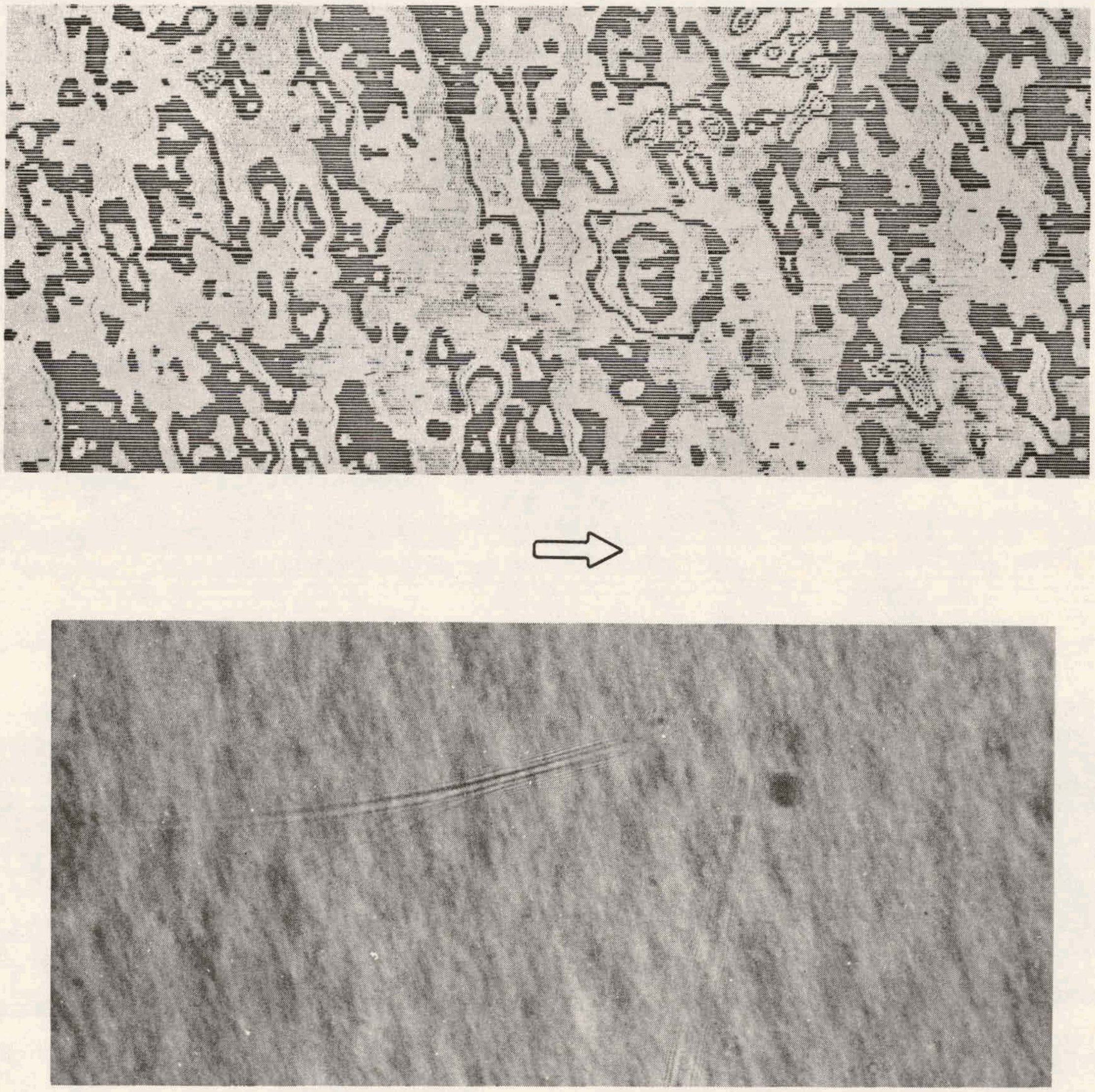

Figure 16 Laser Shadowgraph #1, 380-Micron Gold Microsphere and Isodensity Trace (8B163)

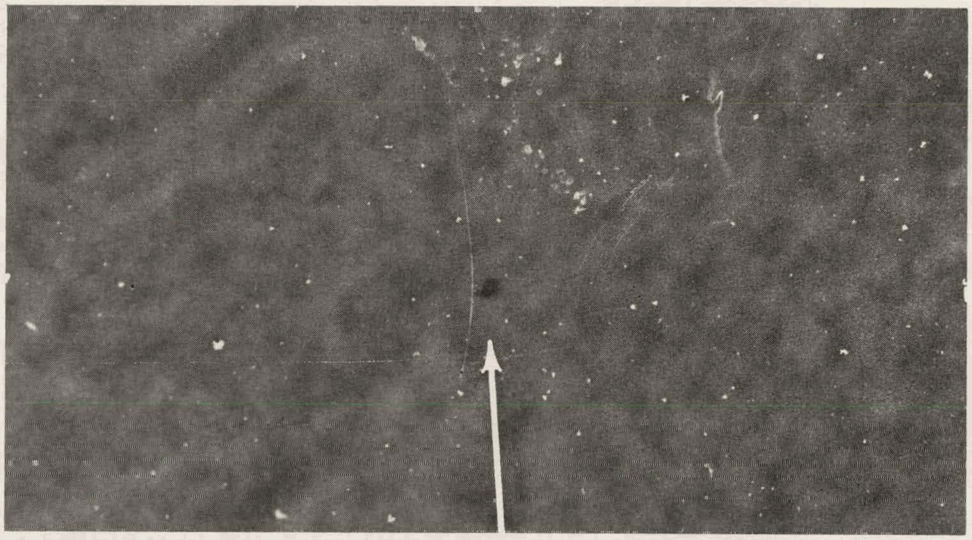

Figure 17 Laser Shadowgraph #1, 250-Micron Gold Microsphere (8B233)

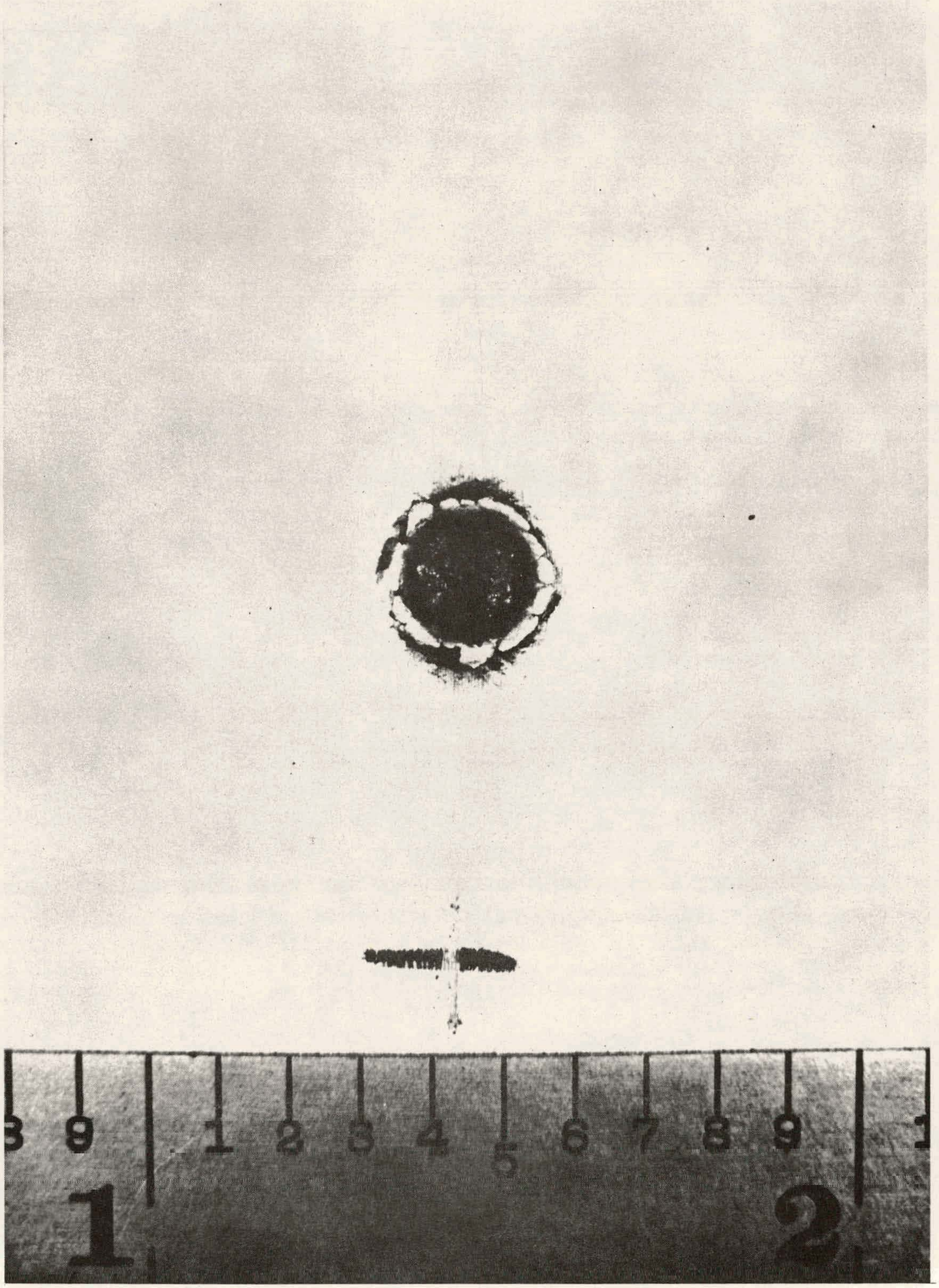

Figure 18 Impact Plate — 520-Micron Gold (8B161)

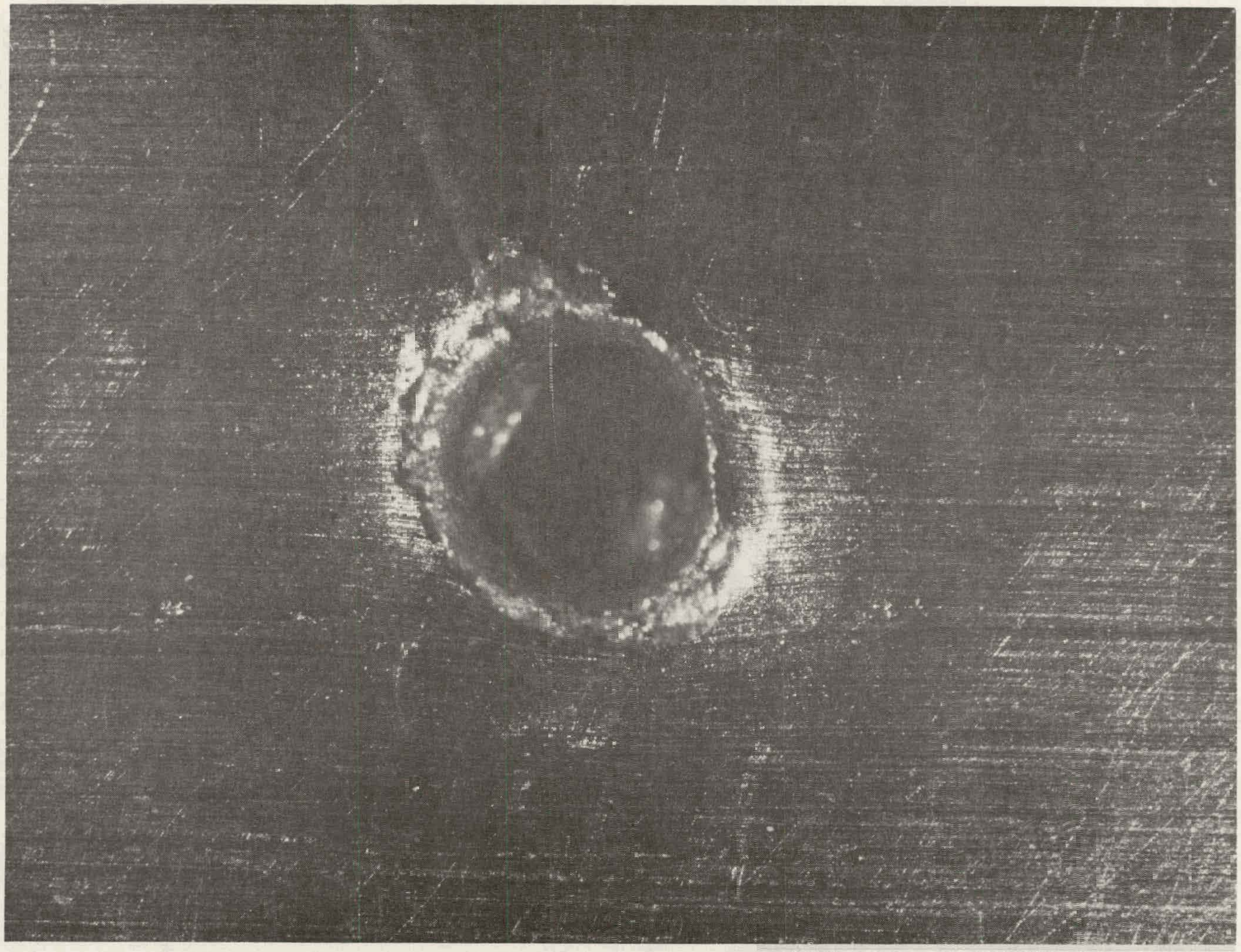

SANDIA CORPORATION PHOTOGRAPH

Figure 19 Impact Plate — 350-Micron Gold (8B216)

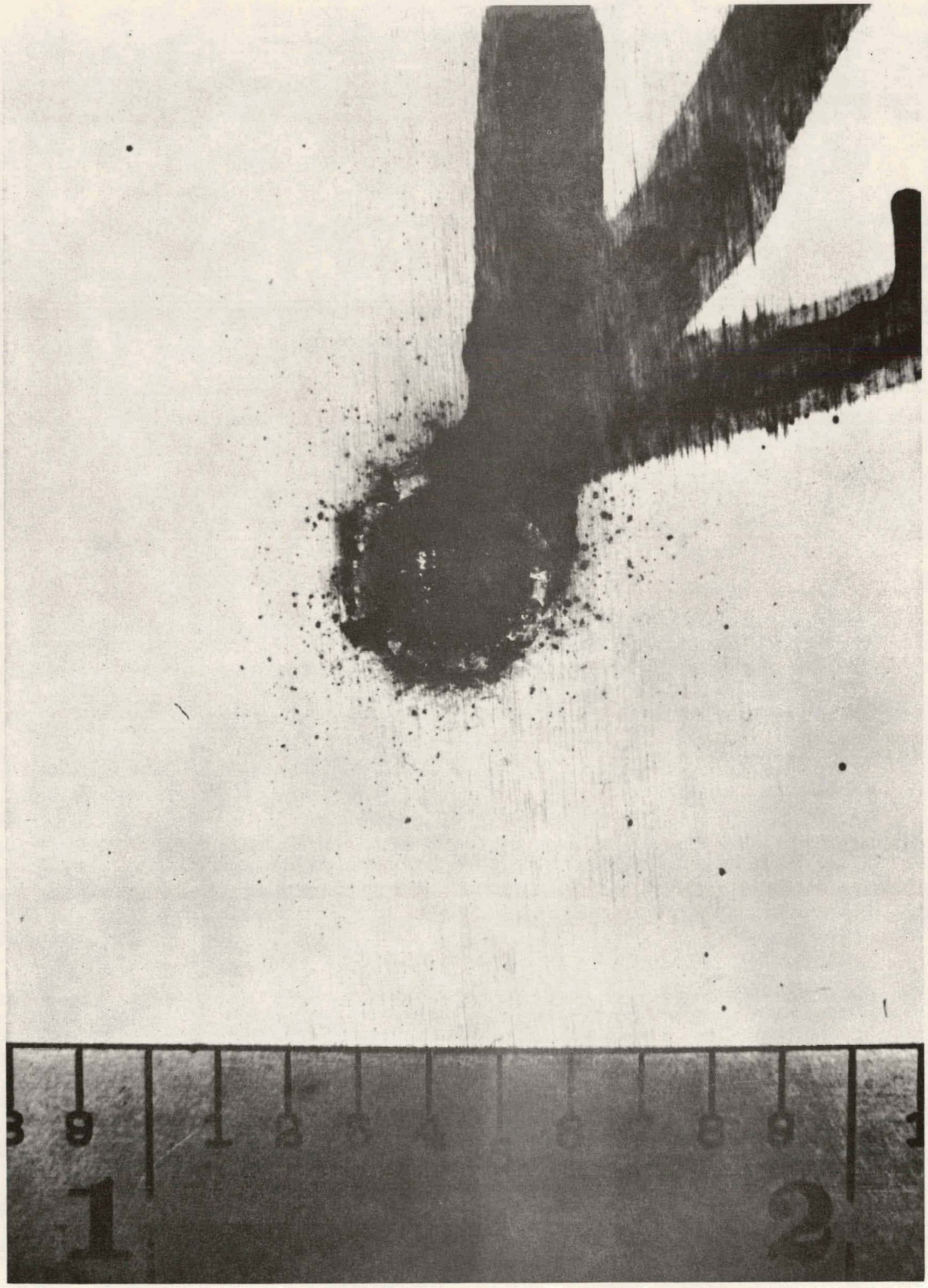

Figure 20 Impact Plate — 650-Micron Gold (8B157)

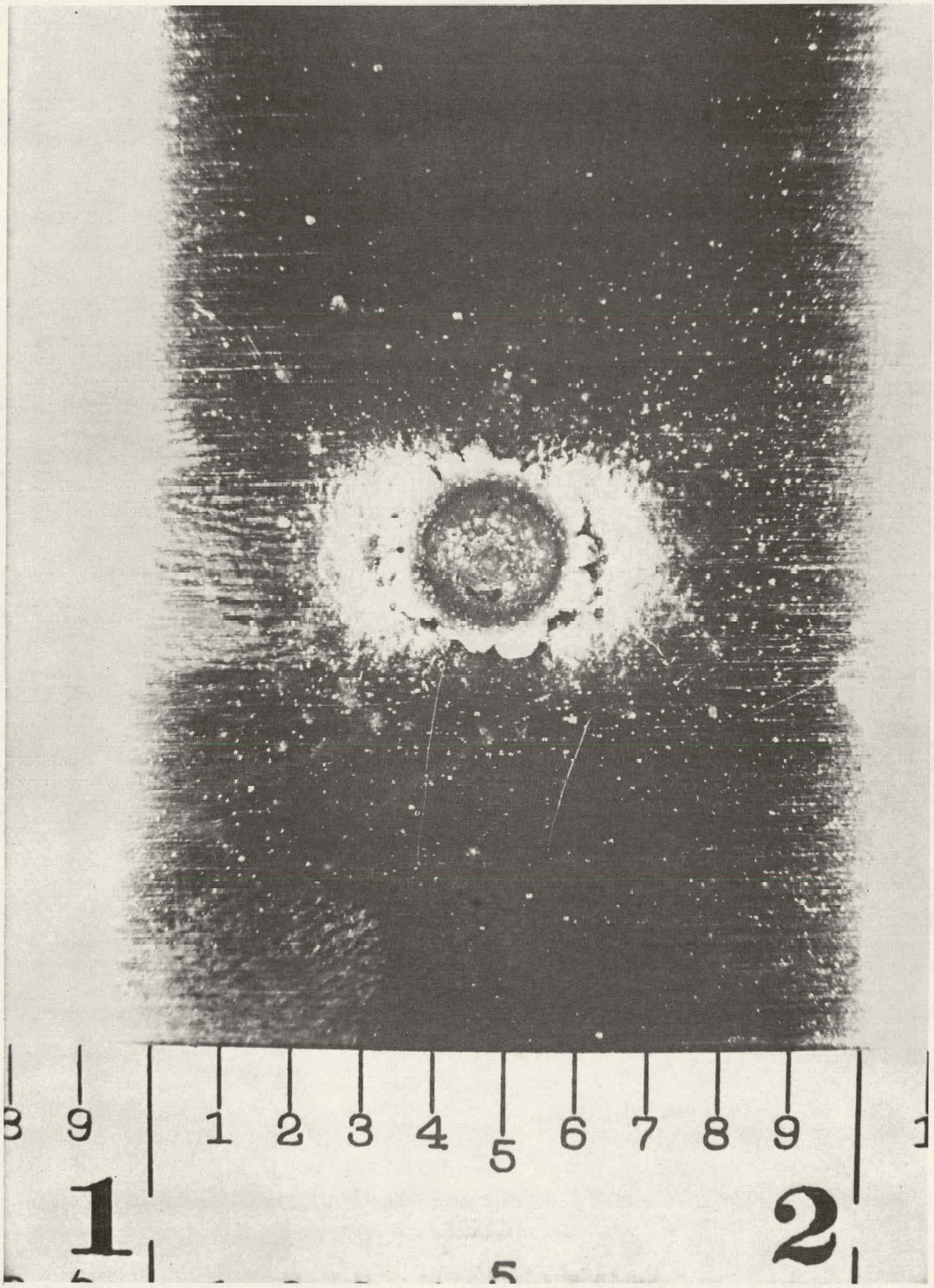

Figure 21 Impact Plate — 650-Micron Gold (8B158)

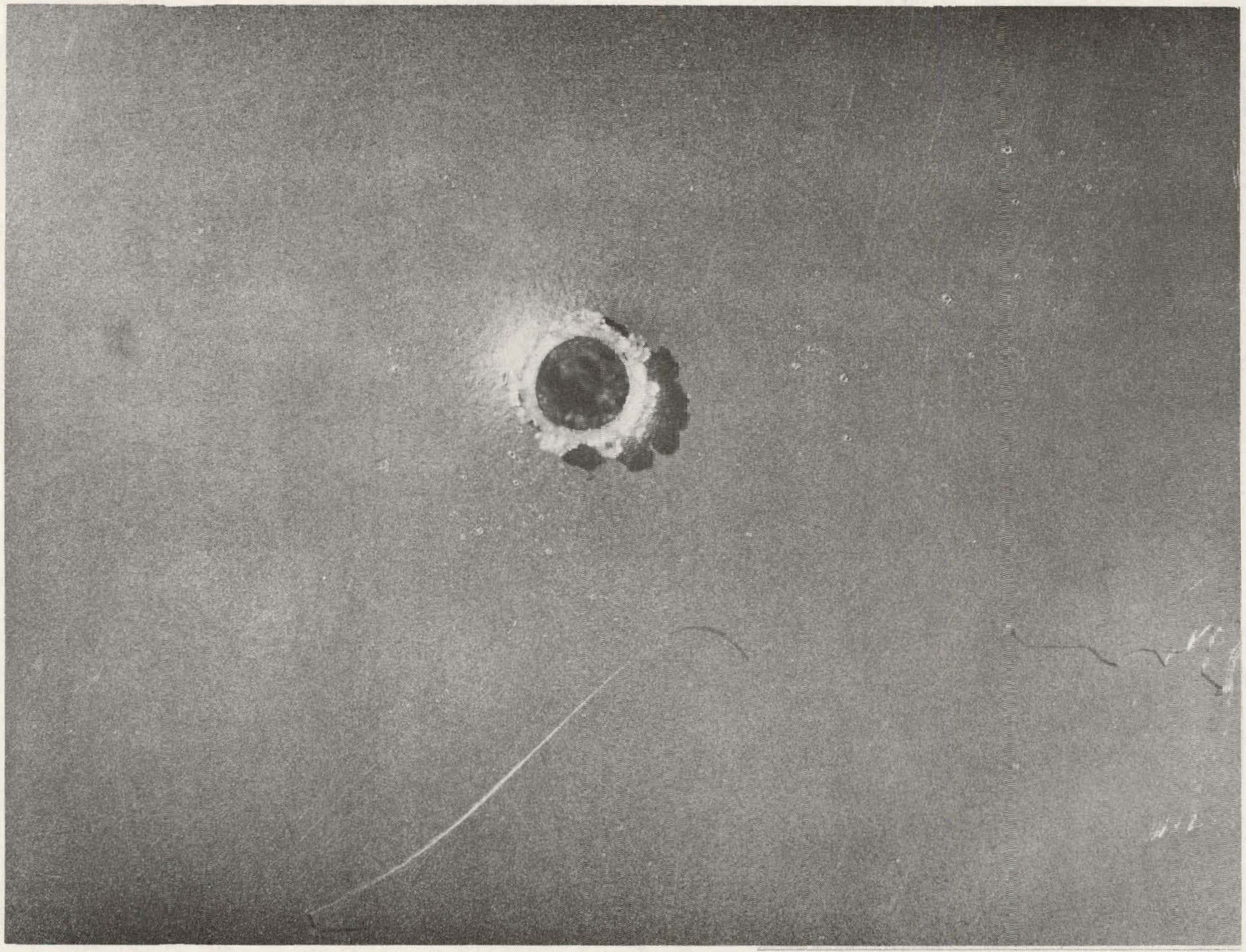

SANDIA CORPORATION PHOTOGRAPH

Figure 22 Impact Plate – 380-Micron Gold (8B220)

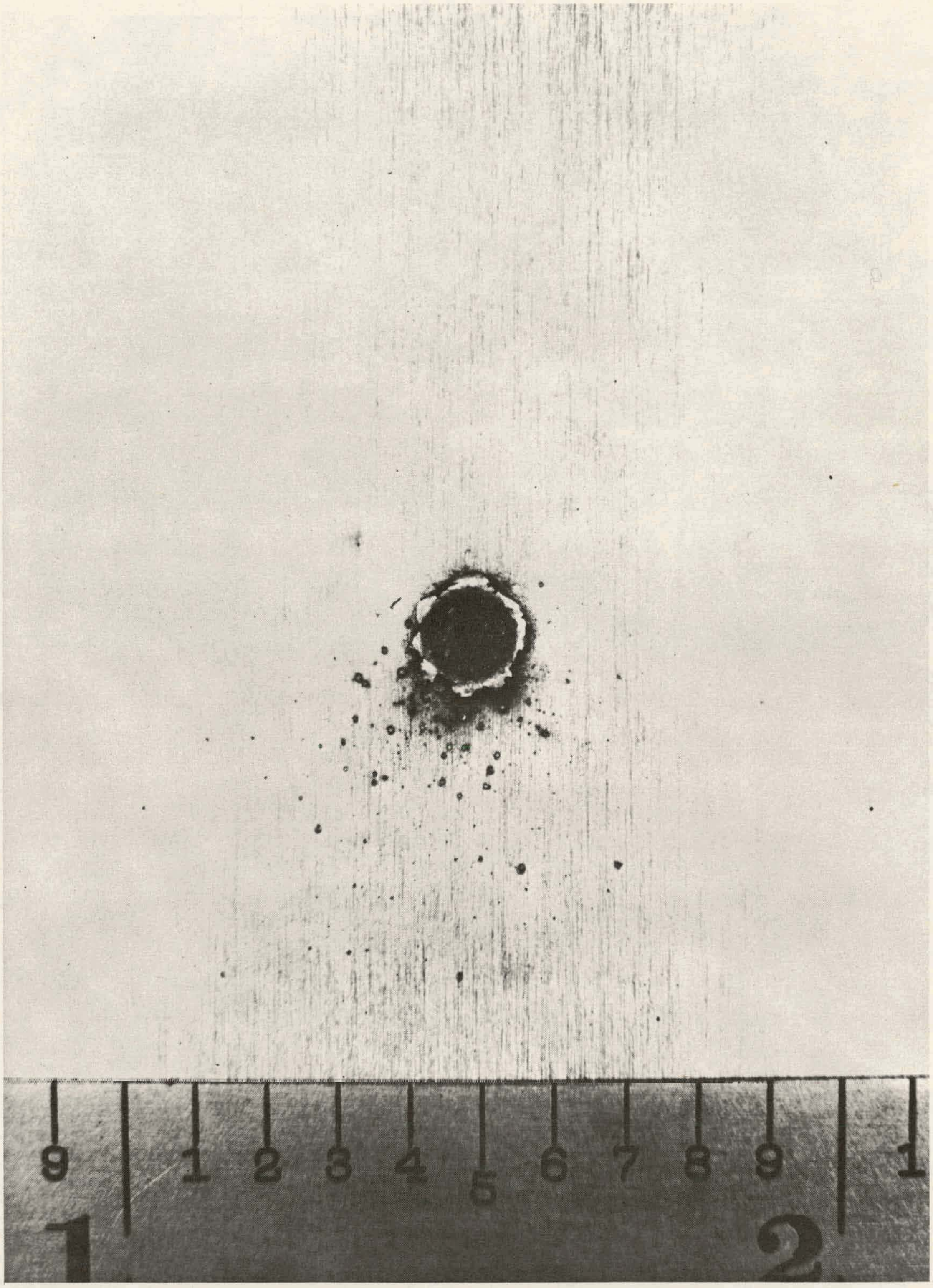

Figure 23 Impact Plate — 380-Micron Gold (8B163)

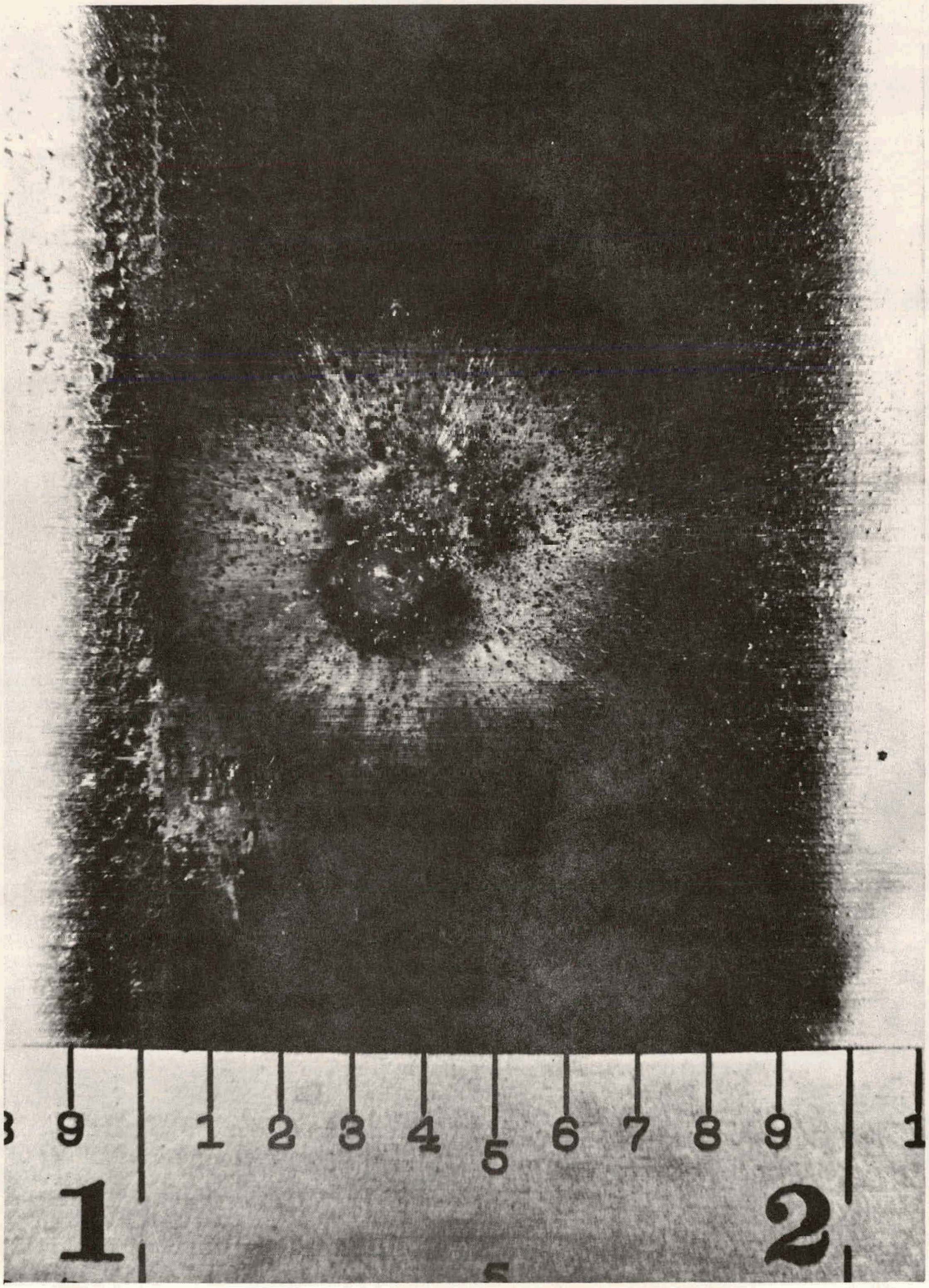

Figure 24 Impact Plate — 380-Micron Gold (8B159)

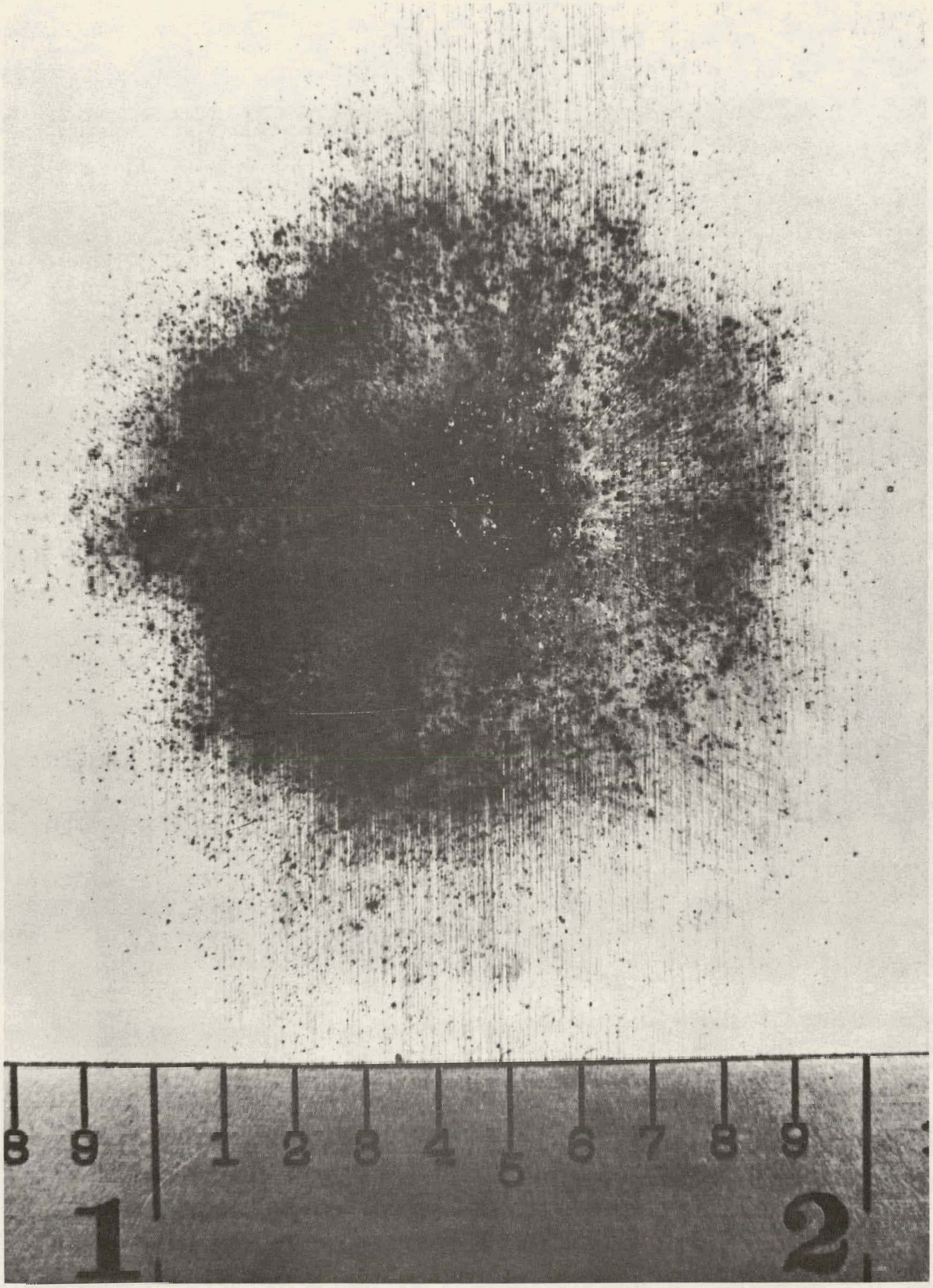

Figure 25 Impact Plate — 380-Micron Gold (8B160)

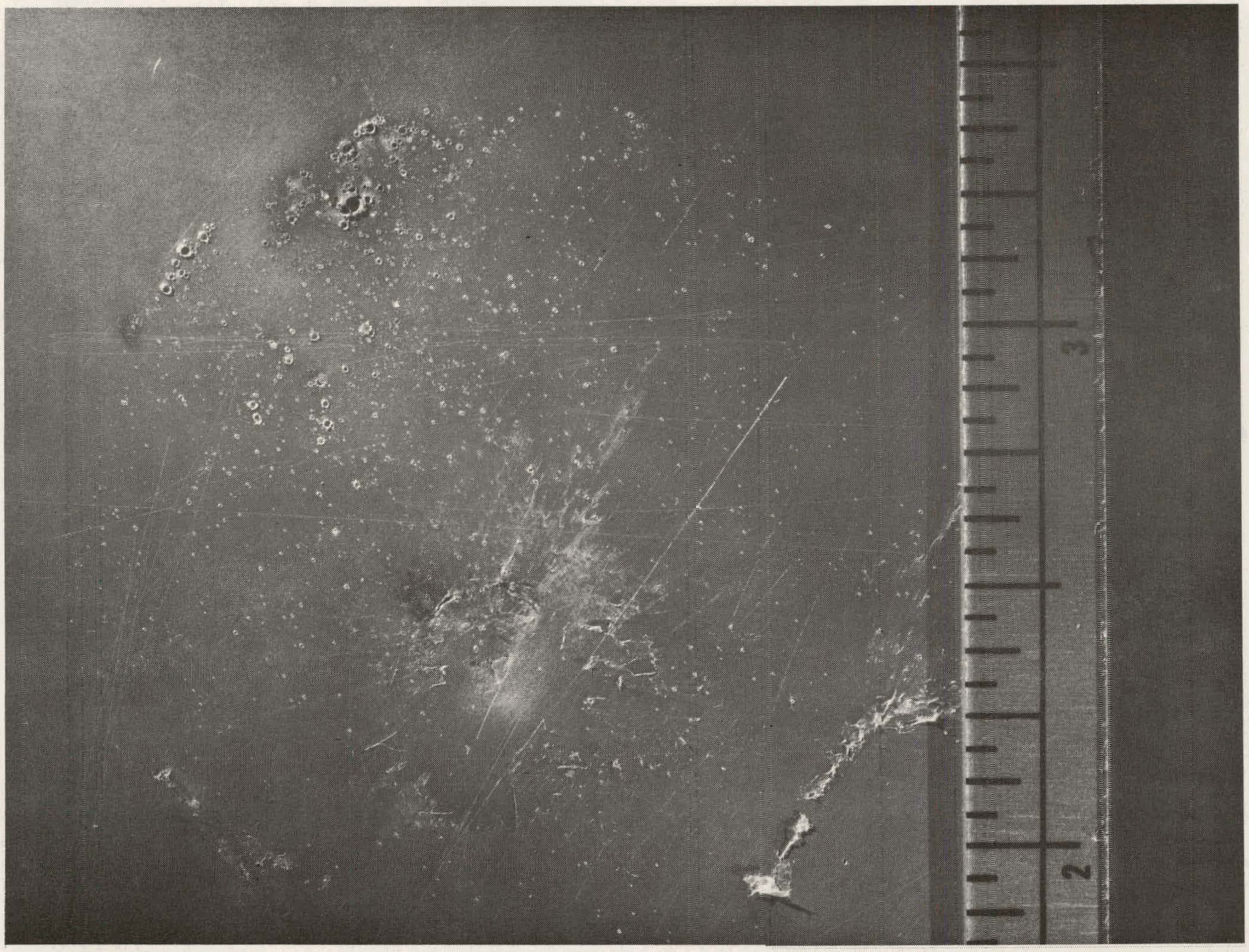

SANDIA CORPORATION PHOTOGRAPH

Figure 26 Impact Plate — 380-Micron Gold (3B217)

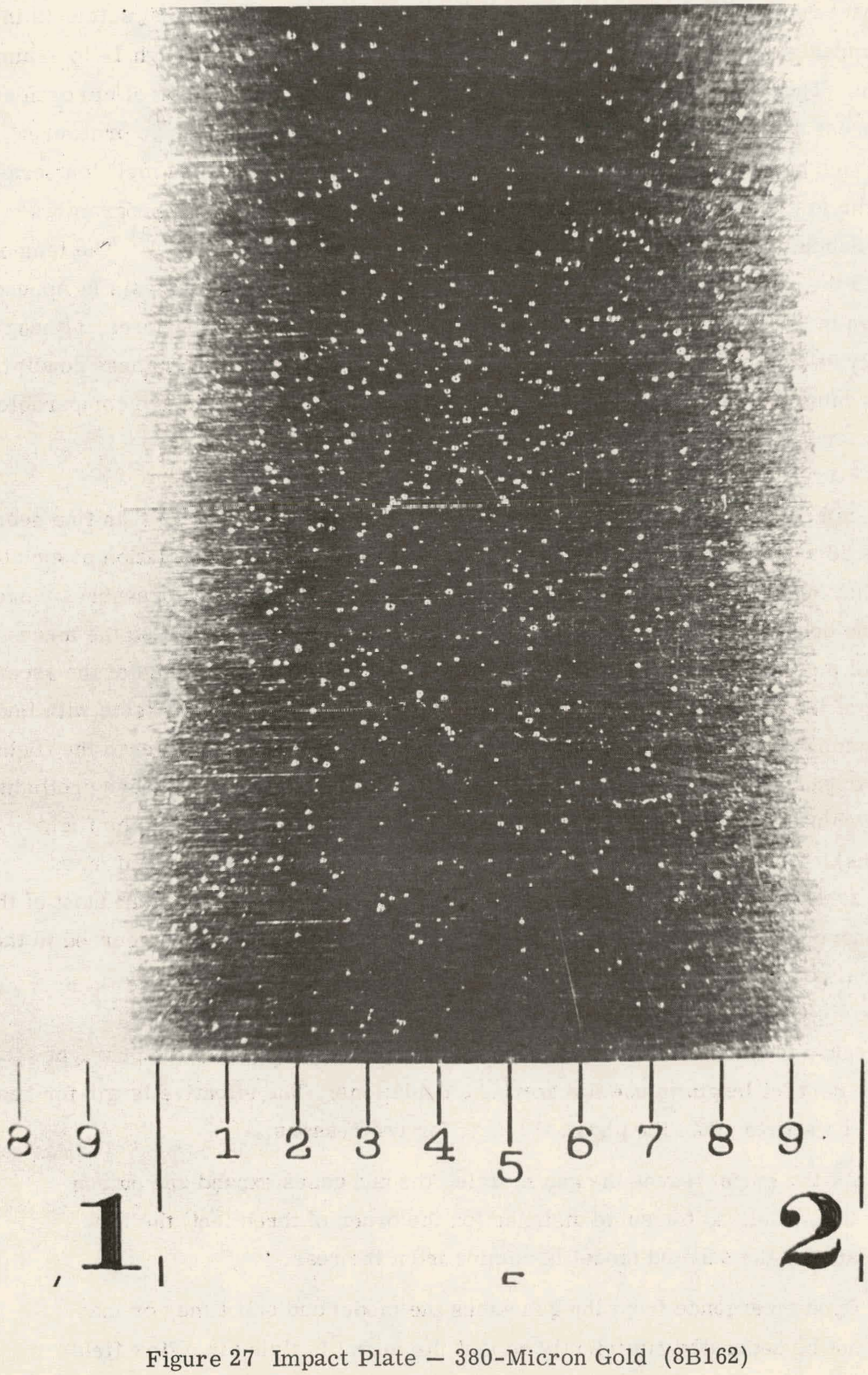

Figure 27 Impact Plate — 380-Micron Gold (8B162)

The impact records of gold microspheres from the third and fourth test setments included impacts of 380- and 250-micron gold microspheres flown through 1- to 4-mm Hg of air. These microspheres were flown through a preflight section of nitrogen at higher pressures so as to pre-heat the microsphere. Free-flight range pressures were chosen by Sandia such that the front of the microsphere reached melt temperature in the low pressure section. A two-dimensional heat conduction program was used by Sandia to analyze aerodynamic heating of these microspheres.(3) The temperatures and the point where surface melt occurs as predicted by the analysis in Appendix A are given in Table VI for the firing conditions of all the gold microspheres, although this analysis was not used in determining the flight conditions. Under these conditions Weber numbers(2) are low and the surface tension forces of the gold are comparable to the shear forces of the hypervelocity flow.

The 250-micron gold microspheres appear to ablate into larger rather than fine debris (Figures 28 and 29 — tests 8B230 and 8B233) as compared with the ablation associated with higher Weber numbers (Figures 20, 21, 22 and 23). At the low pressures more of the fine debris should reach the impact plates if it is produced, and so the mechanisms of mass loss seen in the laser shadowgraphs and impact records of the second segment of tests is not observed, at least in the impact records of the tests with low Weber numbers. Calculations show that some of the microspheres entered the flight section already molten due to an increase in the length of the high pressure preflight section (which was not accounted for in the initial calculations to determine flight conditions). Although no records were obtained to determine the extent of mass ablation at the end of the preflight section, it is reasonable to assume that most of the microsphere entered the flight section intact, and that actual breakup occurred in the flight sections under low Weber number conditions.

In this regard it is well to note that the measured physical length of the preflight section is not the correct length to use for heating calculations. The effective length for heating must be shorter than the physical length for two reasons:

1) As the model leaves the gun muzzle, the gun gases expand and outrun the model, so for some distance (on the order of three feet) the flow around the saboted model is coming from the rear.

2) Upon emergence from the gun gases the model and sabot may or may not be separated sufficiently so that the model is flying in a flow field undisturbed by the sabot pieces. The distance required for sabot

Table VI
ANALYSIS OF TEST CONDITIONS OF GOLD MICROSPHERES

Test No.	Similar Tests	Diameter (microns)	Pressure (Preflight/Flight) (mm Hg)	Initial Velocity (Preflight/Flight) (ft/sec)	Initial Q_{STAG} (BTU/ft^2 sec)	$T_{STAG}=2405^{O}R$ (ft)	$\overline{T}=3340^{O}R$ *	Re	W
8B158	8B157	650	8 Air	21,800	30,500	58	109	3255	171
8B159	8B160	520	7 Air	21,800	31,840	45	83	2278	120
8B161		520	2 Air	21,900	17,270	93	167	654	34.5
8BX46		520	15 N/1 Air	22,300/21,980	50,100/12,350	25	116	5000/328	268/17.3
8B162		380	6 - 7	21,500	34,340	32	55	1525	79
8B217		380	12 N/4 Air	22,150/21,870	51,300/28,450	20	49	2825/954	151/50.3
8B226		380	12 N/4 Air	22,200/21,870	51,800/28,450	20	47	2840/954	152/50.3
8B163		380	2 Air	22,000	20,500	58	94	480	25.4
8B218		380	15 N/1 Air	22,700/22,340	62,220/15,220	11.5	57	3623/244	198/13.1
8B234	8B227	380	15 N/1 Air	22,900/22,475	63,800/15,520	11.5	46	3650/245	201/13.1
8B216 8B223	8B221	380	12 N/1 Air	22,500/22,215	53,950/14,950	19.5	71	2870/242	155/13.0
8B220		380	8 N/1 Air	16,300/16,160	15,750/ 5,820	125	209	1390/176	54.4/6.9
8B233, 8B231	8B230X 8B232	250	7 N/1 Air	22,850/22,550	53,360/19,340	14.5	24.5	1120/162	61.5/8.8
8B235		250	12 N/1 Air	18,200/17,790	33,800/ 9,075	19	43	1527/128	67/5.5

* $3340^{O}R = 2405 + \frac{\text{Heat of Fusion}}{C_p}$ such that when $\overline{T} = 3340^{O}R$, enough heat has entered the microsphere to melt the entire mass.

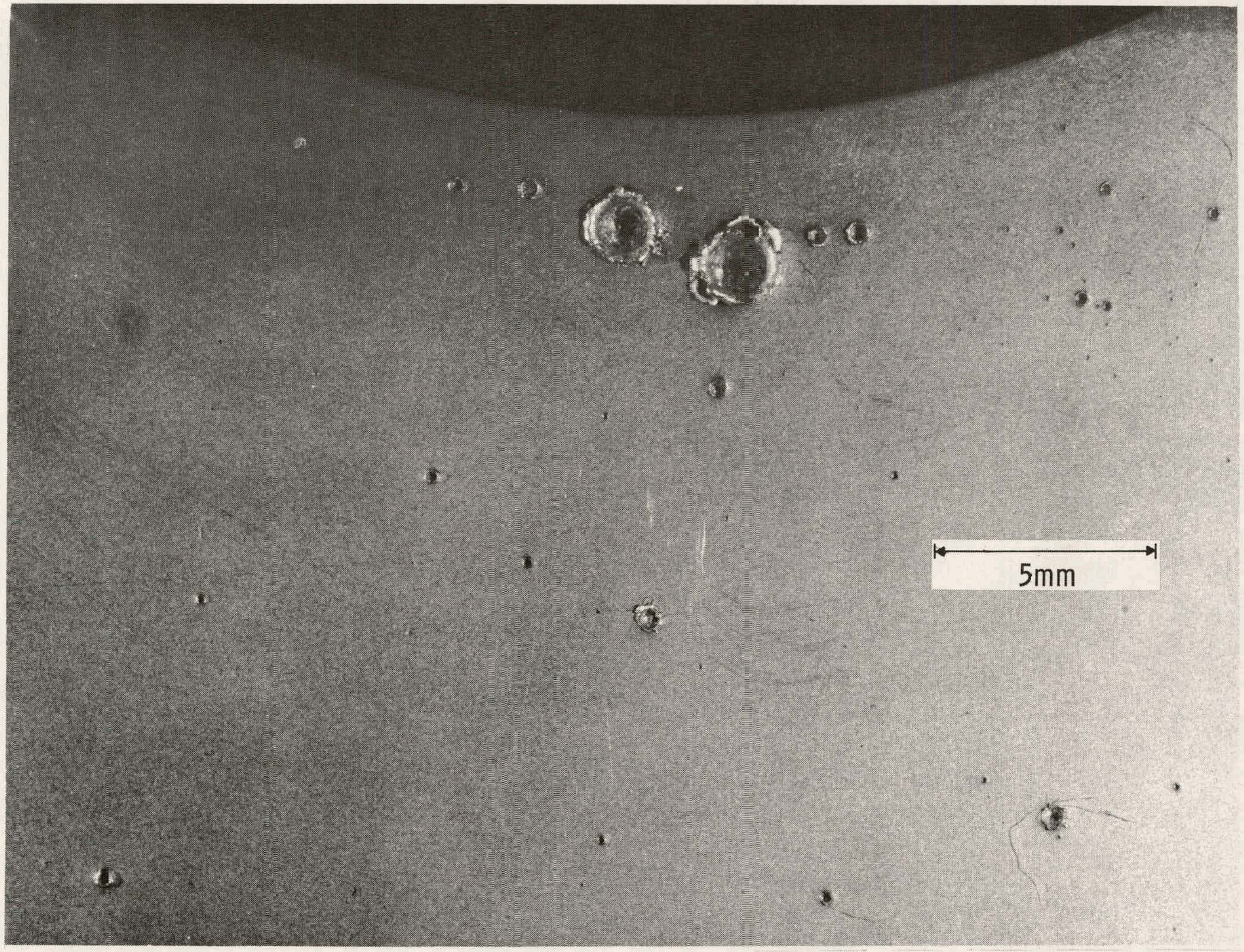

SANDIA CORPORATION PHOTOGRAPH

Figure 23 Impact Plates — 250-Micron Gold (Sandia Photograph) (8B230)

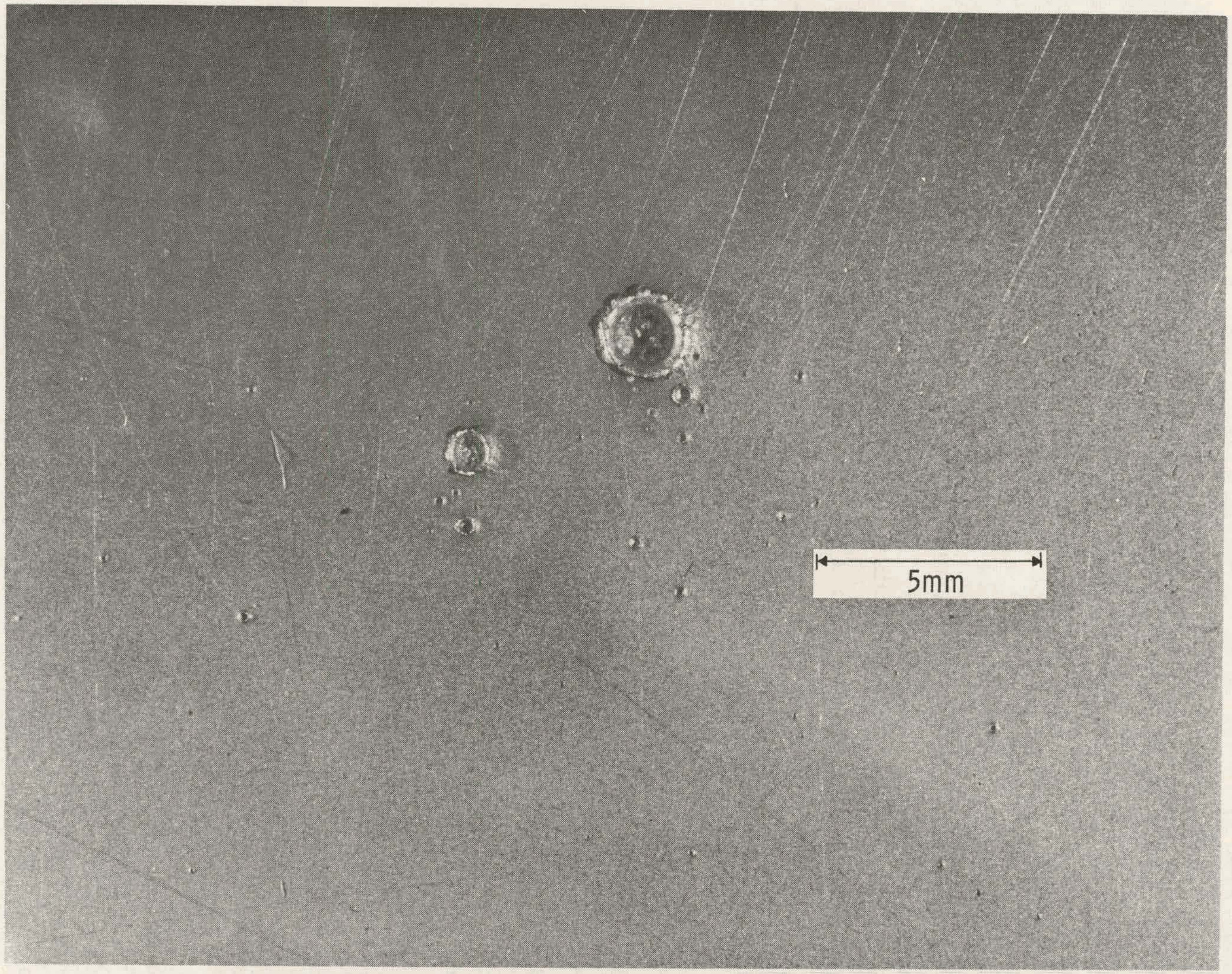

SANDIA CORPORATION PHOTOGRAPH

Figure 29 Impact Plates — 250-Micron Gold (Sandia Photograph) (8B233) separation is a function of preflight pressure and an additional three feet of uncertainty is possible in selecting the correct effective preflight length for heating calculations.

The final conclusions of this experiment relating particle breakup to Weber number will be made by Sandia. Careful measurements of debris impacts and derivation of debris trajectories will indicate whether or not ablation did occur under the low Weber numbers in the flight section.

RECOMMENDATIONS FOR FUTURE WORK

Emphasis should be placed onthe reliability of impact plate data and also on the fact that tests could be conducted with several microspheres at a time. Due to the difficulties in the triggering of one microsphere and of making actual quantitative measurements (as to mass loss and detailed surface measurements) from the laser shadowgraph records of very small microspheres and ablation debris, it appears that the most reliable records of the progressive ablation are to be obtained from successive pass-through impact plates for ablation products, as was done in the last segment of this experiment, and by placing the terminal impact plate at various distances.

Experimental data of a statistical nature as to start of and rate of ablation could be obtained by launching a packet of microspheres and impacting a few of them at a time at various distances. Quantitative analysis could be done by selecting microspheres of the same size, or representative of actual distributions, and placing impactplates and debris collectors to catch all of them. Triggering would be easier and laser shadowgraphs would contain very good records of ablating microspheres (since some would be at the focal distance of the system). A more complete record of the debris cloud of the microspheres could be obtained with a Fraunhofer hologram camera system.(4) Images of the very small ablation debris could be reconstructed and measured. Effects of the number of microspheres per unit volume on ablation and attenuation rates could also be evaluated. For the lighter materials the attenuated ablation debris may be collected and analyzed for size distribution.

REFERENCES

1. D.J. Collins, D.K. Sangster, and W.K. Rogers, "Feasibility Study on Small Particle Ablation Using a Free-Flight Range," Sandia Laboratories, SC-CR-66-2128, Nov 1966.
2. R.E. Lundberg, W.C. Reynolds, and R.A. Rindal, "A Study of the Behavior of Small Particles During Reentry," Sandia Laboratories, SC-CR-67-2635, Jun 1967.
3. C.B. Watkins, "SPHERE 2 A Two Dimensional Heat Conduction and Trajectory Computer Program for Reentry Heating of Small Spherical Bodies," SC-RR-67-2996, Sandia Laboratories, Dec 1967.
4. B.J. Thompson, J.H. Ward, "Particle Sizing — the First Direct Use of Holography," Scientific Research Oct 1966.
5. J.C. Camm, and P.H. Rose, "Electric Shock Tube for High Velocity Simulation," AVCO-Everett Research Report 136, Jul 1962.
6. W.H.T. Loh, "Dynamics and Thermodynamics of Planetary Entry," Prentice Hall, 1963, p. 184.
7. R.A. Matula, "Comparison Between Exact and One-Dimensional Theories for Incipient Melting in Reentry Simulation," ASME Paper No. 65-WA/HT-53, Nov 1965.

APPENDIX A
UNCERTAINTIES ASSOCIATED WITH TWO-PRESSURE RANGE OPERATION

When the range is operated in the two-pressure mode, the high pressure preflight section is separated from the low pressure test section by a port valve which opens rapidly. The possibility therefore exists that shock waves will propagate into the test section. However, at the end of the preflight section, the tank narrows to the sabot-catcher, which for these tests, had a maximum diameter of 1-3/16 inches. The area ratio between the sabot catcher and the 2-foot test section is therefore $(1\text{-}3/16/24)^2 = 408$. In Reference 5, shock attenuation through such an expansion has been calculated in terms of shock-tube parameters. For an initial pressure ratio of 15 (the largest in these tests) and an area ratio of 408, the charts of Reference 5 give the effective pressure ratio for a uniform-bore shock tube of less than unity. Any shock formed at the sabot-catcher will therefore rapidly attenuate to a sound wave in expanding into the test section.

The port valve is not a true high-speed valve in terms of ballistic range times, however, and some flow from preflight into flight chambers will occur during the test time. As an upper bound, it is conservative to estimate that the valve will be fully open for one second before the gun fires. Again, for a conservative first approximation, assume that both tank pressures remain constant. Then the mass flow from the preflight chamber to the flight chamber is given by Fliegner's formula

$$W = 0.532 \frac{A_T p_o}{\sqrt{T_o}} \quad \text{lb/sec for British units.}$$

For one second the flow is $W = 0.74 \times 10^{-2}$ lb. The volume of the preflight chamber is about 64 ft^3 and at 15 torr the gas contained weighs about 9.5×10^{-2} lb. The volume of the flight chamber is about 400 ft^3 and at 1 torr contains about 4.0×10^{-2} lb of air. Therefore:

$$\%\ \text{loss in preflight chamber} \approx \frac{0.74 \times 10^{-2}}{9.5 \times 10^{-2}} \times 100 = 7.8\%$$

$$\%\ \text{gain in flight chamber} \sim \frac{0.74}{4.0 \times 10^{-2}} = 18.5\%.$$

Use of the regular explosively driven fast-acting valve which operates in a few milliseconds would avoid this problem. A fast-acting valve was not used, however, because of cost limitations.

APPENDIX B
THE TEMPERATURES OF AN AERODYNAMICALLY HEATED SPHERE

The stagnation point heating rate of a sphere is assumed to be(6)

$$\dot{Q}_s = 17,000\sqrt{\frac{P_o}{R_n}}\left(\frac{V}{26,000}\right)^{3.19}\left[\frac{\text{BTU}}{\text{ft}^2\cdot\text{sec}}\right] \tag{1}$$

and the heating rate over the front hemisphere is taken to be an approximate function of θ:

$$f(\theta) = \dot{Q}_s \cos\theta \left[\frac{\text{BTU}}{\text{ft}^2\cdot\text{sec}}\right] \tag{2}$$

The total heat entering the sphere per unit time is then

$$\dot{Q}_{TOT} = \int_o^{\pi/2} (\dot{Q}_s \cos\theta)(2\pi R_n \sin\theta)(R_n d\theta) = \pi R_n^2 \dot{Q}_s \left[\frac{\text{BTU}}{\text{sec}}\right] \tag{3}$$

The average temperature of the sphere is then derived by integrating the attenuating heating rate up to time t. The velocity attenuates as follows, assuming constant range pressure and drag coefficient:

$$V(t) = V_o\Big/\left(\frac{V_o\rho t}{2B} + 1\right) \quad [\text{ft/sec}] \tag{4}$$

such that the attenuated heating rate is given by

$$\dot{Q}_s(t) = 17,000\sqrt{\frac{P_o}{R_n}}\left(\frac{V_o}{26000}\right)^{3.19}\left(\frac{1}{\frac{V_o\rho t}{2B} + 1}\right)^{3.19}\left[\frac{\text{BTU}}{\text{ft}^2\cdot\text{sec}}\right] \tag{5}$$

and integrating up to time t

$$Q_s(t) = 17{,}000 \sqrt{\frac{P_o}{R_n}} \left(\frac{V_o}{26000}\right)^{3.19} \frac{2B}{2.19\, V_o \rho} \left(1 - \frac{1}{\left(\frac{V_o \rho t}{2B} + 1\right)^{2.19}}\right) \qquad (6)$$

so the total heat entering the sphere in BTU is

$$Q_{TOT} = 15{,}525 \; \frac{\pi R_n^2 B}{V_o \rho} \sqrt{\frac{P_o}{R_n}} \left(\frac{V_o}{26000}\right)^{3.19} \left(1 - \frac{1}{\left(\frac{V_o \rho t}{2B} + 1\right)^{2.19}}\right) \qquad (7)$$

and the average temperature of the sphere is then

$$\overline{T} = T_o + Q_{TOT} \Big/ \frac{4}{3} \pi R_n^3 \rho_m C_p \qquad (8)$$

We now derive the difference in temperature of the stagnation point and of the back of the sphere from the average temperature. We investigate the asymptotic behavior of the exact solution of the sphere heating problem (7)

$$\frac{T(x, r) - T_o}{\beta} = 3\, C_o \tau + \frac{C_o}{2} (r^2 - 1) + \sum_{n=1}^{\infty} \frac{C_n}{r} P_n(x) + A(\tau, x) \, . \qquad (9)$$

For r = 1 and x = 1, i.e., at the stagnation point, the first three terms in Equation 9 become

$$\frac{T_{STAG} - T_o}{\beta} = \frac{3}{4} \tau + 0.6386 \qquad (10)$$

At the back of the sphere, x = -1, and

$$\frac{T_{BACK} - T_o}{\beta} = \frac{3}{4}\tau - 0.3614 = \frac{T_{STAG} - T_o}{\beta} - 1 . \tag{11}$$

The term $A(\tau, x)$ in Equation (9) yields the transient temperature gradients that occur initially when heat is applied to a sphere of constant temperature, and for the asymptotic solution when τ is greater than 1, this term becomes insignificant. For gold microspheres and materials with high conductivity the asymptotic solution is valid shortly after launch as is seen in Figure B-1, which compares the asymptotic solution with the temperature range in an equivalent thin slab with equivalent heating rates.

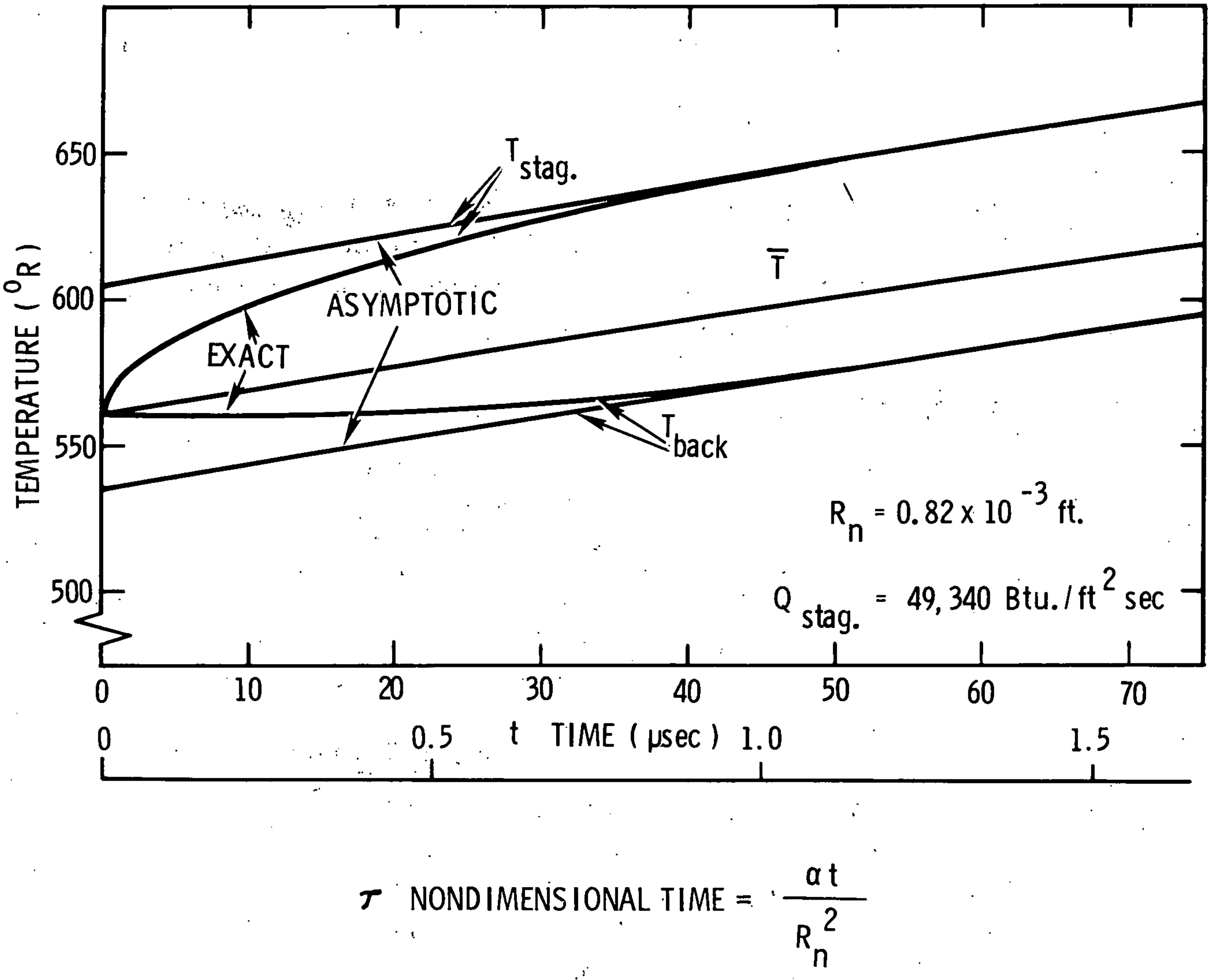

Figure B-1. Comparison of Asymptotic and Exact 1-Dimensional Heating Solution for a Slab

For a 400-micron sintered Al_2O_3 microsphere, with initial velocity 20,000 ft/sec, $t = 1.47$ msec when $\tau = 1$; so the asymptotic solution is valid after 30 ft of flight. Significant temperatures are achieved after the quasi-steady temperature gradient is established.

It is seen that for slowly attenuating heating rates the term

$$\frac{3}{4}\tau = \frac{Q_{TOT}}{\beta \frac{4}{3}\pi R_n^3 \rho_m C_p} \cong \frac{\overline{T} - T_o}{\beta} \tag{12}$$

the back of the sphere are

$$T_{STAG} \cong 0.6386\,\beta + \overline{T} \quad (^{o}R) \tag{13}$$

$$T_{BACK} \cong T_{STAG} - \beta \quad (^{o}R) \tag{14}$$

A simple on-line computer program (Appendix C) has been written to evaluate Equations (1), (4), (8), (13) and (14) for various initial flight conditions. The language is PL/I, as used on the CPS of the IBM-360. Input variables and units are described in the program, and all output is well annotated.

CONSTANTS USED IN ANALYSIS OF TEST CONDITIONS

Density of nitrogen	1.25 gm/ℓ (1 atmos)
Density of air	1.283 gm/ℓ (1 atmos)
μ	3.74×10^{-7} $\frac{\text{lb sec}}{\text{ft}^2}$
Drag coefficient of microspheres	0.9
Initial temperatures	$560^{o}R$
Material properties	

	Gold	Al_2O_3 (Sintered)
Density (lb/ft^3)	1205	222
C_p (BTU/lb ^{o}R)	0.031	0.309
K conductivity (BTU/sec ft ^{o}R)	0.0561	0.02
T melt (^{o}R)	2405	4160
Heat of fussion (BTU/lb)	29	—
Coefficient of surface tension (dyne/cm)	1134	706

APPENDIX C
COMPUTER PROGRAM

```
                  /* PROGRAM TO COMPUTE VELOCITY ATTENUATION
                  /* AND AERODYNAMIC HEATING OF A SPHERE IN
                  /* HYPERVELOCITY FREE-FLIGHT RANGES
                  /* IBM-360 CPS, Programmer: David K Sangster  May 1968
                  /* AC-ELECTRONICS, DEFENSE RESEARCH LABORATORIES
                  /* GENERAL MOTORS CORPORATION, GOLETA, CALIFORNIA
                  ;
                  /*   DESCRIPTION OF INPUT AND UNITS
                  /*      Rhoref: density of gas at STP(gm./ltr)
                  /*      Range: length of free-flight(ft)
                  /*      Csubd: drag coefficient
                  /*      Ttime: time step (sec.) after 0.0005 sec.
                  /*      Stime: time step (sec.) before 0.0005 sec.
                  /*      To: initial sphere temperature(deg. R)
                  /*      Rhomat: density of material (lb/ft**3)
                  /*      Csubp: specific heat (Btu./lb./deg. R)
                  /*      Kcond: conductivity (Btu./sec./ft./deg. R)
                  /*      Tmelt: melt temperature (deg. R)
                  /*      Htfus: heat of sublimation (Btu./lb.)
                  /*      Csurft: surface tension (dynes/cm.)
                  /*      Velo: initial velocity (ft./sec.)
                  /*      Pres: range pressure (mm. Hg)
                  /*      Rspher: radius of sphere (microns)
                  GET LIST(Rhoref,Range,Csubd,Ttime,Stime,To);
                  GET LIST(Rhomat,Csubp,Kcond,Tmelt,Htfus,Csurft);
         start:   GET LIST(Velo,Pres,Rspher);
                  PUT IMAGE(1)(i1);
         i1:      IMAGE;
             FLIGHT DYNAMICS AND HEATING OF A SPHERE;
                  Velokm=Velo*30.48E-05;
                  PUT IMAGE(Velo,Velokm)(i2);
         i2:      IMAGE;
Initial velocity = ------.-- ft./sec. = --.------ km./sec.;
                  Presat=Pres/760;
                  PUT IMAGE(Presat,Pres)(i3);
         i3:      IMAGE;
Range pressure = --.------ atmos.= ------.-- mm. Hg.;
                  Rspin=Rspher*.00003937;
                  Rspft=Rspin/12;
                  PUT IMAGE(Rspft,Rspin,Rspher)(i4);
         i4:      IMAGE;
Sphere radius = --.------ ft. = ---.------ in. = -------.- micron.;
                  Wtlbs=Rhomat*4/3*3.14159*Rspft**3;
                  Wtgms=Wtlbs*453.6;
                  PUT IMAGE(Wtlbs,Wtgms)(i5);
         i5:      IMAGE;
Sphere weight = ......... lb. = ......... gm.;
                  Rhoggm=Presat*Rhoref;
                  Rhoglb=Rhoggm*.06243;
                  PUT IMAGE(Rhoglb,Rhoggm)(i6);
         i6:      IMAGE;
Density of gas = ........ lb./ft.**2 = ........ gm./ltr.;
```

```
  47.            Bcof=Wtlbs/Csubd/(3.14159*Rspft**2);
  48.            Teqv=Tmelt-To+Htfus/Csubp;
  49.            Bcofgm=Bcof*.496;
  50.            PUT IMAGE(Bcof,Bcofgm)(i8);
  51.     i8:    IMAGE;
Ballistic coefficient = ---.--- lb./ft.**2 = ---.--- gm./cm.**2;
  52.            PUT IMAGE(1)(i9);
  53.     i9:    IMAGE;
';
  54.            PUT IMAGE(1)(i10);
  55.     i10:   IMAGE;
 Time       Velocity    Tavg.       Tstag.      Qdots          Re;
  56.            PUT IMAGE(1)(i11);
  57.     i11:   IMAGE;
 (sec.)     (ft./sec.)  (deg. R)    (deg. R) (Btu./(sec.*ft.**2)) **;
  58.            PUT IMAGE(1)(i9);
  59.            PUT IMAGE(1)(i12);
  60.     i12:   IMAGE;
 Distance     Mach    %Eqv. melt    Tback      Qintg.         W;
  61.            PUT IMAGE(1)(i13);
  62.     i13:   IMAGE;
  (ft.)         **         **     (deg. R)   (Btu./ft.**2)     **;
  63.            PUT IMAGE(1)(i9);
  64.            Time=0.;
  65.            Qtotal=15525*SQRT(Presat/Rspft)*(Velo/26000)**3.19;
  66.            Qtotal=Qtotal*Bcof/Velo/Rhoglb;
  67.     loop:  Velot=Velo*Rhoglb*Time/2/Bcof+1;
  68.            Xdist=2*Bcof/Rhoglb*LOG(Velot);
  69.            Velor=Velo/Velot;
  70.            Qdots=17000*SQRT(Presat/Rspft)*(Velor/26000)**3.19;
  71.            Qintg=Qtotal*(1-(Velo*Rhoglb*Time/2/Bcof+1)**-2.19);
  72.            Tavg=To+.75*Qintg/Rspft/Rhomat/Csubp;
  73.            Tstag=Tavg+.6384*Rspft*Qdots/Kcond;
  74.            Tback=Tavg-.3614*Rspft*Qdots/Kcond;
  75.            Reqv=100*(Tavg-To)/Teqv;
  76.            Mach=Velor/1120;
  77.            Re=2*Rspft*Velor*Rhoglb/32.2/3.74E-07;
  78.            Velokm=Velor*30.48E-05;
  79.            W=1E03*Rhoggm*Velokm**2*Rspher/Csurft;
  80.            PUT IMAGE(Time,Velor,Tavg,Tstag,Qdots,Re)(i20);
  81.     i20:   IMAGE;
---.----- ---- ----.- ---------.- ---------.- ---------.-     .........;
  82.            PUT IMAGE(Xdist,Mach,Reqv,Tback,Qintg,W)(i21);
  83.     i21:   IMAGE;
-----.--- ---- --.-- ---------.- ----------.- -------.---     ........;
  84.            PUT IMAGE(1)(i9);
  85.            IF Time<.0005 THEN GO TO before;
  86.            Time=Time+Ttime;
  87.            GO TO check;
  88.     before: Time=Time+Stime;
  89.     check:  IF Xdist<Range THEN GO TO loop;
  90.            GO TO start;
```

DISTRIBUTION:

Standard Distribution
TID-4500 (54th Edition)
UC-36 (177 copies)

U.S. Atomic Energy Commission
Division of Space Nuclear Systems
Space Electric Power Office
Washington, D. C. 20545
Attn: G. A. Newby, Assistant Director
G. P. Dix, Chief,
Safety Branch (1)
R. T. Carpenter, Chief, Isotope
Power Systems Branch (1)
J. A. Powers, Chief, Isotopes
Fuels and Materials Branch (1)
C. E. Johnson, Chief, Reactor
Power Systems Branch (1)

U.S. Atomic Energy Commission
Space Nuclear Propulsion Office
Washington, D. C. 20545

U.S. Atomic Energy Commission
Director of Regulation
Washington, D. C. 20545
Attn: C. K. Beck, Deputy Director
F. D. Anderson, Regulation

U.S. Atomic Energy Commission
Division of Biology and Medicine
Washington, D. C. 20545
Attn: J. Z. Holland
Fallout Studies Branch
H. D. Bruner, Asst. Director
Medical and Health Research

U.S. Atomic Energy Commission
Space Nuclear Propulsion Office
Albuquerque Extension
Albuquerque Operations Office
P.O. Box 5400
Albuquerque, New Mexico 87115
Attn: H. P. Smith

U.S. Atomic Energy Commission
Albuquerque Operations Office
P.O. Box 5400
Albuquerque, New Mexico 87115
Attn: B. W. Colston, Director,
Non-Weapons Act. Division
For: J. Nicks
J. F. Burke, Director,
Operational Safety Division

AEC Site Representative
National Aeronautics and Space Adm.
Manned Space Center
Houston, Texas 77058
Attn: W. C. Remini
Bldg. 17, Code ZS-5

Deputy I.G. for Insp. & Safety, USAF
Kirtland Air Force Base,
New Mexico 87117
Attn: Col. D.C. Jameson (AFINSR)

Jet Propulsion Laboratory
California Institute of Technology
4800 Oak Grove Drive
Pasadena, California 91103
Attn: A. L. Klascius, Radiation
Health and Safety

Los Alamos Scientific Laboratory
P.O. Box 1663
Los Alamos, New Mexico 87544
Attn: Dr. L.D.P. King
Dr. Wright Langham
C. F. Metz, CMB-1
F. W. Schonfeld, CMF-5
J. A. Leary, CMB-11

Monsanto Research Corporation
Mound Laboratory
P.O. Box 32
Miamisburg, Ohio 45342
Attn: G. R. Grove

DISTRIBUTION: (Cont.)

Thomas B. Kerr
Code RNS
National Aeronautics and Space Administration
Washington, D. C. 20545

National Aeronautics and Space Administration
Ames Research Center
Moffett Field, California
Attn: Glenn Goodwin

U.S. Naval Radiological Defense Lab.
San Francisco, California 94135
Attn: S. Z. Mikhail, Nuclear Systems Group

National Aeronautics and Space Administration
Goddard Space Flight Center
Glen Dale Road
Greenbelt, Maryland 20771
Attn: A. W. Fihelly, Nimbus Project

Naval Facilities Engineering Command
Department of the Navy, Code 042
Washington, D. C. 20390
Attn: Graham Hagey

Space Nuclear Propulsion Office
Lewis Research Center
21000 Brookpark Road
Cleveland, Ohio 44135
Attn: L. Nichols

Union Carbide Corporation
Nuclear Division
P.O. Box X
Oak Ridge, Tennessee 37831
Attn: R. A. Robinson, Isotope Development Center
B. R. Fish, Health Physics Division

U.S. Public Health Service
Nat. CTR for Radiological Health
1901 Chapman Avenue
Rockville, Maryland 20852
Attn: Nuclear Facilities Section

AC Electronics
Defense Res. Labs.
General Motors Corp.
Santa Barbara, California (10)

Dr. D. W. Sherwood
National Aeronautics and Space Administration
Manned Spacecraft Center (MSC-TD)
Houston, Texas 77058

D. B. Shuster, 1200
L. E. Lamkin, 7300
G. A. Fowler, 9000
R. C. Maydew, 9320
L. A. Hopkins, Jr., 9500
A. J. Clark, Jr., 9510
J. D. Shreve, 9511
S. L. Jeffers, 9512
S. McAlees, Jr., 9513
J. D. Appel, 9514
J. D. Appel, 9514 (ARPIC) (2)
R. J. Everett, 9515
G. J. Hildebrandt, 9520
J. W. McKiernan, 9521
J. Jacobs, 9522
B. F. Hefley, 8232 (5)
R. S. Gillespie, 3411
For: M. S. Goldstein
DTIE (2)
J. L. Gardner, 3421
C. H. Sproul, 3428-2 (10)